AGU PUBLICATIONS

JGR

Journal of Geophysical Research: Atmospheres

RESEARCH ARTICLE

10.1002/2013JD020731

Key Points:
- Satellite observations of gravity waves (GWs) show QBO-related variations
- In the tropics observed GW drag agrees well with the missing drag in ERA-Interim
- GW observations hint at uncertainties in modeled advection terms

Correspondence to:
M. Ern,
m.ern@fz-juelich.de

Citation:
Ern, M., F. Ploeger, P. Preusse, J. C. Gille, L. J. Gray, S. Kalisch, M. G. Mlynczak, J. M. Russell III, and M. Riese (2014), Interaction of gravity waves with the QBO: A satellite perspective, *J. Geophys. Res. Atmos.*, *119*, 2329–2355, doi:10.1002/2013JD020731.

Received 14 AUG 2013
Accepted 12 FEB 2014
Accepted article online 13 FEB 2014
Published online 14 MAR 2014

Interaction of gravity waves with the QBO: A satellite perspective

M. Ern[1], F. Ploeger[1], P. Preusse[1], J. C. Gille[2,3], L. J. Gray[4], S. Kalisch[1], M. G. Mlynczak[5], J. M. Russell III[6], and M. Riese[1]

[1]Institut für Energie- und Klimaforschung – Stratosphäre (IEK–7), Forschungszentrum Jülich GmbH, Jülich, Germany, [2]Center for Limb Atmospheric Sounding, University of Colorado Boulder, Boulder, Colorado, USA, [3]National Center for Atmospheric Research, Boulder, Colorado, USA, [4]Atmospheric Physics, Department of Physics, University of Oxford, Oxford, UK, [5]NASA Langley Research Center, Hampton, Virginia, USA, [6]Center for Atmospheric Sciences, Hampton University, Hampton, Virginia, USA

Abstract One of the most important dynamical processes in the tropical stratosphere is the quasi-biennial oscillation (QBO) of the zonal wind. Still, the QBO is not well represented in weather and climate models. To improve the representation of the QBO in the models, a better understanding of the driving of the QBO by atmospheric waves is required. In particular, the contribution of gravity waves is highly uncertain because of the small horizontal scales involved, and there is still no direct estimation based on global observations. We derive gravity wave momentum fluxes from temperature observations of the satellite instruments HIRDLS and SABER. Momentum flux spectra observed show that particularly gravity waves with intrinsic phase speeds <30 m/s (vertical wavelengths <10 km) interact with the QBO. Gravity wave drag is estimated from vertical gradients of observed momentum fluxes and compared to the missing drag in the tropical momentum budget of ERA-Interim. We find reasonably good agreement between their variations with time and in their approximate magnitudes. Absolute values of observed and ERA-Interim missing drag are about equal during QBO eastward wind shear. During westward wind shear, however, observations are about 2 times lower than ERA-Interim missing drag. This could hint at uncertainties in the advection terms in ERA-Interim. The strong intermittency of gravity waves we find in the tropics might play an important role for the formation of the QBO and may have important implications for the parameterization of gravity waves in global models.

1. Introduction

The quasi-biennial oscillation (QBO) is an oscillation of the zonal wind in the tropical stratosphere with an average period of about 28 months. QBO westward winds can be as strong as about 40 m/s, while maximum QBO eastward winds are considerably weaker (about 20 m/s). An overview of the QBO and its effects are given, for example, by *Baldwin et al.* [2001].

The QBO is an important process in atmospheric dynamics, and effects of the QBO are found over a large range of altitudes and also in the extratropics. For example, the QBO has influence on the frequency of stratospheric warmings in the Northern Hemisphere polar vortex [*Holton and Tan*, 1980]. It has been argued by *Holton and Tan* [1980] that the polar vortex should be more stable if the QBO zonal wind at the 50 mbar pressure level (about 21 km altitude) and the wind in the polar vortex have the same direction (i.e., eastward) and less stable during QBO westward phases when the winds are opposite. The QBO also influences the weather and climate in the extratropical lower atmosphere and even at the surface [e.g., *Ebdon*, 1975; *Boer and Hamilton*, 2008; *Marshall and Scaife*, 2009], and complicated interactions between the QBO and the 11 year solar cycle affect the global circulation over a large range of latitudes [e.g., *Gray et al.*, 2010, and references therein]. Further, by wind filtering, the QBO influences the spectrum of waves that propagate upward. This has an effect on the atmospheric circulation patterns at higher altitudes. For example, the prefiltered wave spectrum is likely responsible for the formation of a QBO in the tropical mesopause region [see also *Baldwin et al.*, 2001, and references therein].

It has been proposed by *Lindzen and Holton* [1968] and *Holton and Lindzen* [1972] that the QBO is a wave-driven circulation pattern. In particular, this is indicated by the downward propagation of the QBO eastward and westward wind phases with time. Meanwhile, it has been accepted that both global-scale

waves and short horizontal scale gravity waves contribute. Gravity waves cover a large range of relatively short horizontal wavelengths (from several tens to a few thousand kilometers). In the equatorial region most of the driving by waves that are usually resolved in models is due to equatorial wave modes, for example, Kelvin waves, mixed Rossby-gravity waves, and equatorial Rossby waves. These resolved waves, particularly the Kelvin waves, can have considerable temperature amplitudes of several kelvins and zonal wind amplitudes of several m/s in the stratosphere [e.g., *Ratnam et al.*, 2006; *Ern et al.*, 2008, 2009b; *Yang et al.*, 2012], but nonetheless the wave driving by these global-scale waves is not sufficient, and it has been concluded that gravity waves account for most of the driving of the QBO [e.g., *Dunkerton*, 1997; *Ern and Preusse*, 2009a, 2009b; *Evan et al.*, 2012]. However, the direct quantification of the relative importance of global-scale waves and gravity waves for the driving of the QBO is still an open issue.

Because of its importance for the dynamics of the whole atmosphere, much effort has been made to simulate a QBO, as realistically as possible, in general circulation models (GCMs) and chemistry-climate models (CCMs) [e.g., *Scaife et al.*, 2000; *Giorgetta et al.*, 2002, 2006; *Kawatani et al.*, 2010; *Orr et al.*, 2010; *Xue et al.*, 2012]. Given its relevance for the surface weather and climate at high northern latitudes, a realistic model-generated QBO possibly would allow more accurate longer-range weather predictions, as well as climate predictions that are robust not only on global average, but also on regional scales [e.g., *Boer and Hamilton*, 2008; *Gerber et al.*, 2012]. The simulated QBO in GCMs/CCMs is, however, often not fully realistic in its wind amplitude and oscillation period. One major shortcoming of the models is the representation of atmospheric waves that contribute to the driving of the QBO. Usually, global-scale waves with long vertical wavelengths can be simulated in GCMs/CCMs. However, often the vertical resolution of the models is too coarse to reliably resolve waves with short vertical wavelengths (both planetary-scale waves and gravity waves), as well as the propagation and wave-mean flow interactions of waves in general. Also, limitations in the horizontal resolution are a major problem. In particular, gravity waves are too short in their horizontal scales and are underestimated in global models [e.g., *Schroeder et al.*, 2009]. For this reason, GCMs/CCMs usually require parameterized gravity wave drag to drive the QBO, which involves large uncertainties.

To obtain a more realistic QBO in GCMs/CCMs, an improvement of the parameterized gravity wave drag is required. For this purpose, global observations of gravity waves are needed (i.e., observations from satellite) [e.g., *Alexander et al.*, 2010; *Geller et al.*, 2013]. In particular, global observations of gravity waves can be used to directly estimate the relative importance of global-scale waves and gravity waves for the driving of the QBO. This information is required to adjust the strength of the parameterized gravity wave momentum flux in GCMs/CCMs to obtain the correct amount of gravity wave drag in the tropical stratosphere. There are also indications that the intermittency of gravity wave sources might play an important role for the dynamics of the QBO and that this intermittency should be included in gravity wave parameterizations [*Lott et al.*, 2012]. Further, it is important to find out which part of the gravity wave spectrum contributes to the driving of the QBO. Global observations of gravity wave momentum flux and drag, as well as gravity wave spectra and intermittency, are therefore important information that can support efforts of modeling a realistic QBO. Such observations are also a step toward attributing observed gravity waves to particular source processes, and, provided that these sources are correctly parameterized in GCMs/CCMs [see also, for example, *Song et al.*, 2007; *Richter et al.*, 2010; *Kim et al.*, 2013], the information could help to account for feedback processes like changing gravity wave sources in a changing climate.

Even though global observations of gravity waves from satellites are difficult because of the short horizontal scales of those waves, several studies show that gravity wave activity in the tropics is modulated by the QBO [e.g., *de la Torre et al.*, 2006; *Krebsbach and Preusse*, 2007; *Ern et al.*, 2008; *Wu and Eckermann*, 2008]. These studies are, however, limited to gravity wave variances or squared amplitudes, and no spectral information about horizontal and vertical wavelengths of the gravity waves that drive the QBO was obtained. Moreover, these previous studies did not provide gravity wave momentum fluxes and gravity wave drag that would have been needed to estimate the contribution of gravity waves to the QBO driving. In several previous studies gravity wave momentum fluxes and gravity wave drag derived from High Resolution Dynamics Limb Sounder (HIRDLS) and Sounding of the Atmosphere Using Broadband Emission Radiometry (SABER) observations have already provided valuable information about the interaction of gravity waves with the background flow [e.g., *Alexander et al.*, 2008; *Wright et al.*, 2010; *Ern et al.*, 2011, 2013b]. Therefore, in our study we use these data sets to investigate also the interaction of gravity waves with the QBO in the tropics. In particular, for the first time the contribution of gravity wave drag to the forcing of the QBO is estimated directly from satellite observations of gravity wave momentum flux in the tropics.

In section 2 the data sets used in our study are described, and in section 3 we investigate how the global distribution of gravity waves observed by the satellite instruments HIRDLS and SABER is modulated by the QBO. From the satellite observations we calculate gravity wave momentum flux spectra in the tropics to identify the part of the momentum flux spectrum that is responsible for the driving of the QBO (see Appendix B). In section 3 we also directly estimate gravity wave drag from the satellite observations to learn more about the forcing of the QBO by gravity waves. For this purpose the observed gravity wave drag is compared to the amount of wave drag that is missing in the momentum budget of the European Centre for Medium-Range Weather Forecasts (ECMWF) ERA-Interim reanalysis. In addition, the intermittency of gravity wave momentum fluxes in the tropics is estimated from the satellite observations. Finally, a summary and discussion is given in section 4.

2. Data Sets Used

2.1. The Instruments HIRDLS and SABER

HIRDLS is one of the instruments onboard the EOS Aura satellite. For more than 3 years (January 2005 until March 2008) HIRDLS observed mid-infrared emissions of trace species in limb-viewing geometry. From emissions of CO_2 molecules around 15 μm atmospheric temperature-pressure profiles are derived from the tropopause region to above 70 km altitude. The vertical field of view (FOV) of the HIRDLS instrument is 1 km. This value is preserved for the vertical resolution of observed temperature altitude profiles. This is possible because measurement noise is low and because the FOV is 5 times vertically oversampled during altitude scans. The vertical resolution of 1 km for HIRDLS altitude profiles has been confirmed in several studies [e.g., *Barnett et al.*, 2008; *Gille et al.*, 2008; *Wright et al.*, 2011]. The horizontal distance between subsequent altitude profiles is about 100 km. These horizontal and vertical resolutions are very advantageous for the analysis of small-scale atmospheric structures, such as gravity waves. The latitudinal coverage of HIRDLS is from about 63°S to 80°N. In our study we use version V006 HIRDLS temperatures [see also *Gille et al.*, 2011]. In the observed temperature altitude profiles we analyze temperature fluctuations that are induced by gravity waves. Therefore, only random errors (precision), and not systematic errors (accuracy), of the derived temperatures are important for us. (For example, minor systematic temperature biases will not affect the temperature fluctuations that can be attributed to gravity waves.) Typical random errors of HIRDLS temperatures (measured standard deviations) are ∼0.3 K at 20 km altitude, increasing to ∼0.6 K at 50 km [see *Gille et al.*, 2011, Figure 5.1.3]. These values are well below the zonal average standard deviations that we attribute to gravity waves (see section 3.1). More information about the HIRDLS instrument and temperature retrieval is available, for example, in *Gille et al.* [2003, 2008, and references therein].

The SABER instrument is one of the instruments onboard the Thermosphere-Ionosphere-Mesosphere Energetics and Dynamics (TIMED) satellite. Like the HIRDLS instrument, temperature altitude profiles are derived from CO_2 limb radiances. Temperatures are derived from the tropopause region to well above 100 km altitude with an altitude resolution of about 2 km. This value is very close to the vertical FOV of the SABER instrument and is also achieved by low measurement noise and 5 times vertically oversampling the FOV during vertical scans, similarly as for HIRDLS. For both HIRDLS and SABER the inherently narrow weighting functions in the limb preserve the vertical resolution afforded by the FOV. For SABER the horizontal sampling step between subsequent altitude profiles is between about 200 and 600 km, depending on the triangular vertical scanning pattern [see also *Remsberg et al.*, 2008]. The TIMED satellite performs yaw maneuvers about every 60 days. Therefore, SABER switches every about 60 days between a northward and a southward viewing geometry with latitudinal coverages of about 50°S–82°N and 82°S–50°N, respectively. SABER observations started in January 2002 and are still ongoing at the time of writing. Our study is based on SABER v1.07 temperature data. The random error (precision) of SABER temperatures is ∼0.3 K below about 32 km altitude, increasing to ∼0.6 K at 40 km altitude [see *Remsberg et al.*, 2008, Table 1]. Like for HIRDLS, these values are well below the standard deviations due to gravity waves (see section 3.1). More information about the SABER instrument and temperature retrieval is available in *Mlynczak* [1997], *Russell et al.* [1999], and *Remsberg et al.* [2004, 2008, and references therein].

2.2. Estimation of Gravity Wave Variances, Momentum Fluxes, and Drag From Satellite Observations

In order to investigate the interaction of the global distribution of gravity waves with the QBO, we derive gravity wave variances, momentum fluxes, and drag from HIRDLS and SABER temperature observations. We always consider averages over the latitude band 10°S–10°N and 7 days in time with a time step of 3 days. This provides both good statistics and a time resolution that is sufficient to sample the very short periods of

strong QBO wind shear. The extraction of gravity waves and their characteristics from temperature altitude profiles observed from satellite is a procedure that involves several data processing steps. This procedure is described in more detail in *Ern et al.* [2004, 2011] and is only briefly summarized here.

2.2.1. Estimation of Gravity Wave Variances

First, the zonal mean background state of the atmosphere is removed from the altitude profiles. Then the temperature field due to global-scale waves is determined by carrying out a space-time spectral decomposition in longitude and time for a set of fixed latitudes and altitudes. The latitude step used is 1° for both instruments, and the altitude step is 0.5 km for HIRDLS and 1 km for SABER. Latitude and altitude ranges of this latitude/altitude grid were chosen according to the global coverage of the two instruments. The space-time spectra were determined in overlapping time windows of 31 days length. These spectra are used to reconstruct the superposition of global-scale waves for the exact coordinates in space and time of each temperature observation for the HIRDLS and SABER instrument, respectively. For more details see also *Ern et al.* [2011, 2013b].

The orbit geometry of satellites in low Earth orbit resolves zonal wave numbers of about 7, depending on the ground-based frequency of the waves. By combining ascending and descending parts of the satellite orbit, global-scale waves with periods as short as about 1 day can be resolved. However, we only use zonal wave numbers up to 6 and wave frequencies <0.7 cycles/d for the removal of global-scale waves. In the equatorial region it is important to use a large range of wave frequencies because Kelvin waves, the most dominant global-scale equatorial wave mode in temperatures, can have very short wave periods of only a few days, even in the stratosphere [e.g., *Forbes et al.*, 2009; *Ern et al.*, 2008, 2009a; *Ern and Preusse*, 2009a]. In addition to the procedure as described in *Ern et al.* [2011] also the strongest tidal modes have been removed by subtracting quasi-stationary zonal wave numbers 0–4, separately for ascending and descending parts of the satellite orbits [see also *Ern et al.*, 2013b].

2.2.2. Estimation of Gravity Wave Momentum Flux Absolute Values

Having removed the global-scale waves, the results are altitude profiles of residual temperatures that can be attributed to mesoscale gravity waves. For these altitude profiles the dominant vertical wave structures (strongest waves) are determined by a combination of maximum entropy method and harmonical analysis (MEM/HA), as described in *Preusse et al.* [2002, sections 3.2 and 3.3]. The outcomes of this procedure are altitude profiles of amplitudes and vertical wavelengths and phases (these phases define the location of the sinusoid in the vertical direction) of the strongest waves for each altitude profile of residual temperatures. This technique uses vertical windows of fixed vertical extent to determine the gravity wave parameters. In our current study we use vertical windows of 10 km for gravity wave momentum flux spectra in order to cover a vertical wavelength range as large as possible (2–25 km). For all other purposes we determine total (absolute) gravity wave momentum fluxes using narrower windows of 5 km vertical extent in order to obtain an altitude resolution as fine as possible but with a smaller available range of vertical wavelengths (2–12 km). In order to minimize the influence of longer vertical wavelengths outside this range on the analysis results, the data are high-pass filtered (in vertical wave number m) by applying a fast Fourier transform (FFT) to the entire vertical profile. The high-pass filtered altitude profiles are obtained by carrying out the back-transformation only for vertical wavelengths λ_z <12 km ($m = 2\pi/\lambda_z$). The capabilities of the MEM/HA method are illustrated for several altitude profiles in Appendix A.

According to estimates of the uncertainty in the observed vertical wavelengths [see *Preusse et al.*, 2002], we assume that in two consecutive altitude profiles of the satellite measurement track (profile pairs) the same wave is observed if the vertical wavelengths differ by no more than 40%. For the analysis with the 10 km vertical window, between 60 and 70% of the pairs are retained in the tropics. For the high-pass filtered data set with the narrower 5 km window, around 80% of the pairs are retained. The selection of profile pairs does not alter average distributions of gravity wave variances in either case, for example, the zonal mean variance. This means that the average variance of selected profile pairs is approximately equal to the variance of all profiles, and the resulting momentum fluxes are therefore likely representative for the average distribution of gravity waves [see also *Geller et al.*, 2013].

If in a pair of altitude profiles the same wave is observed, the horizontal wavelength can be estimated from the vertical phase shift of the wave between the two profiles. Of course, this horizontal wavelength estimate represents only the projection of the true wavelength on the measurement track and is therefore always an overestimation of the true horizontal wavelength. This is discussed in more detail by *Preusse et al.* [2009]. To be able to determine the horizontal wavelength, it is required that the horizontal distance between the

two profiles is below about 300 km. Since the two profiles are measured within less than 40 s, the phase difference between the profiles can be attributed to the horizontal wave structure alone. The 300 km criterion is fulfilled for almost all HIRDLS pairs of altitude profiles and for about 50% of the SABER profile pairs (for details see *Ern et al.* [2011]).

Once we have determined the horizontal wavelength, the absolute momentum flux F_{ph} carried by the wave can be estimated via equation (7) in *Ern et al.* [2004]:

$$F_{ph} = \frac{1}{2}\,\varrho_0\,\frac{\lambda_z}{\lambda_h}\left(\frac{g}{N}\right)^2\left(\frac{\hat{T}}{T}\right)^2 \tag{1}$$

with ϱ_0 the atmospheric background density, g the gravity acceleration, N the buoyancy frequency, λ_h and λ_z the horizontal and vertical wavelength of the gravity wave, $\hat{T}$ the temperature amplitude of the wave, and T the atmospheric background temperature.

For this approach we assume that in each altitude profile there is one wave dominating over the others. This is usually a good approximation. For our study this is even more the case: after application of the vertical wave number high-pass filter (only vertical wavelengths <12 km are retained), at a given altitude contributions of waves other than the strongest one can be neglected.

Since no directional information can be recovered from the 2D information provided by a single satellite measurement track, these momentum fluxes are only absolute momentum fluxes. If averaged over a region, the resulting average momentum fluxes can be considered an average over the momentum flux absolute values of all horizontal propagation directions of the observed gravity waves. Since we are not able to account for cancellation effects of gravity waves carrying momentum in opposite directions, we call these momentum fluxes also "total" momentum fluxes. This shortcoming has to be accounted for when comparing gravity wave momentum flux observations with momentum fluxes from models [see also *Geller et al.*, 2013].

The uncertainty of these absolute (total) momentum fluxes is large, at least a factor of 2. Sometimes net momentum fluxes could be even close to 0 due to cancellation effects, while total or absolute momentum fluxes could be sizable [see also *Geller et al.*, 2013, Appendix B]. On the other hand, if in a region the momentum fluxes of the observed gravity waves have predominantly the same direction, total and net momentum fluxes will be about the same.

One main error source of observed absolute (total) momentum flux is the horizontal wavelength, but also the observational filter of the instrument contributes. Satellite instruments using the limb-viewing geometry can only detect gravity waves with horizontal wavelengths longer than about 100–200 km and vertical wavelengths (λ_z) longer than about twice the vertical field of view. Accordingly, HIRDLS is able to detect gravity waves with λ_z >2 km and SABER with λ_z >4–5 km. Of course, close to the detection limits at short horizontal and vertical wavelengths, the sensitivity of the instruments for temperature fluctuations is strongly reduced, resulting in an underestimation of wave amplitudes [see also *Preusse et al.*, 2002, 2009; *Ungermann et al.*, 2010].

From the single gravity wave momentum flux observations, it is also possible to determine momentum flux spectra (momentum flux as a function of horizontal and vertical wave number) if we subdivide the plane of horizontal and vertical wave numbers into bins and integrate over the momentum fluxes of the single observations falling into each bin. Of course, this is only possible if we consider a larger number of observations in a certain longitude/latitude region [see also *Lehmann et al.*, 2012]. For the display of these spectra it is advantageous to use logarithmic scales for both horizontal and vertical wave numbers. The procedure for estimating gravity wave spectra is described in more detail in *Ern and Preusse* [2012].

2.2.3. Estimation of Total Gravity Wave Drag

From vertical gradients of total (absolute) momentum flux the total (absolute) drag XY on the background wind due to gravity waves can be calculated as follows:

$$XY = -\frac{1}{\varrho_0}\frac{\partial F_{ph}}{\partial z} \tag{2}$$

with XY the acceleration or deceleration of the background wind and z the vertical coordinate.

However, since the total (absolute) momentum flux F_{ph} as described above does not contain any directional information, also the values of wave drag *XY* calculated from its vertical gradients represent only total drag (i.e., absolute values) [see also *Ern et al.*, 2011]. Like the total momentum fluxes, estimates of total gravity wave drag have large uncertainties, at least a factor of 2. In particular, "total drag" is an unphysical quantity, and "net drag" resulting from vertical gradients in "net momentum fluxes" would be needed to describe the effect of gravity waves on the background flow. Like for total momentum flux, total drag could be sizable, while net drag could be close to 0. Total drag and net drag are the same only if the momentum flux of the observed gravity waves has prevailingly the same direction.

Under certain meteorological conditions it is possible to overcome the lack of directional information: in strong wind jets and directly above, it can be assumed that the total momentum flux is dominated by gravity waves propagating opposite to the prevailing wind direction in the jet, and the resulting total gravity wave drag should have a decelerating effect on the wind jet, especially in regions of strong vertical wind shear at the top of the jet. This has been discussed in much detail in *Warner et al.* [2005] and *Ern et al.* [2008, 2011, 2013b]. Also, observations confirm that gravity wave momentum fluxes in wind jets are preferentially directed opposite to the background wind [e.g., *Gong et al.*, 2008]. Further, *Ern et al.* [2013b] have shown that based on this assumption, meaningful results can be achieved and a consistent picture of the breakdown of the summertime mesospheric zonal wind jet is obtained. It can be expected that also for other situations this assumption holds.

Of course, wind jets can also have meridional components. Usually, however, the zonal direction is by far dominant. Therefore, in our study we assume that observed total gravity wave drag can mainly be attributed to the zonal direction and that uncertainties due to meridional components in the wind jets are small compared to other error sources. In particular, *Warner et al.* [2005] have shown that also for the tropical wind jets of the QBO the dominant component of the momentum flux and the resulting wave drag should be directed opposite to the prevailing zonal winds. In our study this assumption indeed leads to a consistent picture of the dynamics of the QBO; see below.

It should, however, be mentioned that our data set of observed gravity wave momentum fluxes covers only a limited part of the whole spectrum (only horizontal wavelengths >100–200 km and vertical wavelengths <25 km). It has been found by *Geller et al.* [2013] that momentum flux vertical gradients in global models are weaker than in limb observations from satellite. It has been argued that short horizontal wavelength gravity waves (λ_h <100 km, not visible for the limb sounders) should dissipate at higher altitudes than longer horizontal wavelength gravity waves. This could lead to the difference in vertical gradients. However, the real reason for this difference is still not fully understood, and there are several effects that may contribute: If it is assumed that the gravity wave momentum flux phase speed spectrum is the same for short and long horizontal wavelength gravity waves, long horizontal wavelength gravity waves should have larger amplitudes (cf. equation (1)) and should therefore saturate earlier, in particular potentially before reaching a critical level. Another explanation for the different vertical gradients could be, for example, that the gravity wave momentum flux phase speed spectrum might be different for short and long horizontal wavelength gravity waves.

Of course, gravity wave momentum fluxes and gravity wave drag derived in our study are only representative of the part of the gravity wave spectrum contained in our observations. To account for the full effect of gravity waves in driving the QBO, also the dissipation of waves in the unobserved part of the gravity wave spectrum would have to be considered. It can, however, be speculated that if short horizontal wavelength gravity waves on average deposit momentum at higher altitudes, already a significant part of the driving of the QBO is covered by our data set.

Another shortcoming is that close to their critical level the vertical wavelengths of dissipating gravity waves become very short, and already somewhat below their critical level they are no longer observable by the satellite instruments. On the other hand, this shortcoming is helpful, because we are able to reliably determine amplitudes, vertical wavelengths, and momentum fluxes until close to the altitudes where these waves become invisible for the satellite instruments. Please note that the 5 km vertical window of our analysis is not much longer than the shortest vertical wavelengths that are usually observed by the satellite instruments (about 3 km for HIRDLS and about 5 km for SABER), and variations of the vertical wavelengths with altitude can therefore be captured. It is also important that the MEM/HA method as described by *Preusse et al.* [2002] is a two-stage method: the best fit wave is determined in a fixed vertical window for a set of

predefined vertical wavelengths. Therefore, this method offers a better altitude resolution than just a simple Fourier analysis (see also Appendix A).

With the 5 km vertical window used in our study, reasonable momentum fluxes can be determined already a few km below and above the altitude where a dissipating wave becomes invisible, and the 5 km vertical window provides an effective smoothing and interpolation for the altitude range in between. This interpolation will somewhat increase the already very large errors, but our momentum fluxes and their vertical gradients will still provide useful information. Of course, when comparing to model data, we have to account for the limited vertical resolution of our data, as well as for the systematical shift in altitude arising from the observational filter of the instruments.

2.3. The Zonal Momentum Balance in ERA-Interim

2.3.1. Background

For comparison with the wave drag estimated directly from observations, we determine the momentum balance in the tropics from meteorological data, similarly to what was done in *Ern and Preusse* [2009a, 2009b]. For this purpose we use the ECMWF ERA-Interim data set [e.g., *Dee et al.*, 2011]. In the lower and middle stratosphere this data set should be quite reliable due to the assimilation of a large number of observations complemented by a good underlying model, good quality control, and good analysis procedures. For details on the ERA-Interim data assimilation system see *Dee et al.* [2011, and references therein].

A high-quality assimilation of data is essential to obtain realistic distributions of temperatures and winds. For example, if no data are assimilated, the ECMWF model version used for ERA-Interim (forecast model version Cy31r2 from December 2006) does not simulate a QBO. The likely reason for this shortcoming is the poor parameterization of gravity wave drag by a Rayleigh friction scheme. Only in more recent model versions, starting with the forecast model version Cy35r3, which became operational in September 2009, the ECMWF model is able to self-generate a QBO. This improvement was achieved by replacing the Rayleigh friction scheme by a spectral parameterization of gravity waves [*Orr et al.*, 2010].

Another benefit of data assimilation is that in ECMWF analyses and reanalyses the planetary waves are also quite realistic. For example, good agreement of planetary waves has been found by comparison with satellite observations in the tropical lower and middle stratosphere [e.g., *Ern et al.*, 2008, 2009b]. There is also good agreement of wave drag due to Kelvin waves in the tropics between ECMWF and satellite observations [e.g., *Ern and Preusse*, 2009a, 2009b]. A good representation of planetary waves in ERA-Interim is important for us because in this subsection we calculate the missing drag in the ERA-Interim tropical zonal momentum budget. Since the planetary waves in ERA-Interim are quite realistic, we can assume that this missing drag can be attributed mainly to gravity waves.

For determining the zonal momentum budget, we use ERA-Interim data with a time step of 6 h, which is important to avoid biases by diurnal cycle effects [e.g., *Seviour et al.*, 2012]. Our ERA-Interim data are on a horizontal grid of $1° \times 1°$ in longitude and latitude. The altitude resolution is about 1.4 km. The transformed Eulerian mean (TEM) zonal momentum equation can be expressed as follows [see also *Andrews et al.*, 1987]:

$$\frac{\partial \overline{u}}{\partial t} + \overline{v}^* \left(\frac{\left(\overline{u}\cos\Phi\right)_\Phi}{a\cos\Phi} - f \right) + \overline{w}^* \overline{u}_z = \overline{X}_{PW} + \overline{X}_{GW} \tag{3}$$

In this equation $\partial\overline{u}/\partial t$ is the tendency of the zonal mean zonal wind $\overline{u}$, f the Coriolis frequency, $\overline{v}^*$ and $\overline{w}^*$ the TEM meridional and vertical wind, a the Earth's radius, Φ the geographic latitude, and $\overline{X}_{PW}$ and $\overline{X}_{GW}$ the zonal mean zonal wave drag due to planetary and gravity waves, respectively. Subscripts Φ and z indicate differentiation in meridional and vertical direction, respectively. Overbars indicate zonal averages. In the following, the momentum budget terms involving $\overline{v}^*$ and $\overline{w}^*$ will be called "meridional advection term" and "vertical advection term," respectively.

The TEM zonal mean meridional and vertical winds are defined as follows:

$$\overline{v}^* = \overline{v} - \frac{1}{\varrho_0} \left(\varrho_0 \frac{\overline{v'\Theta'}}{\overline{\Theta}_z} \right)_z \tag{4}$$

$$\overline{w}^* = \overline{w} + \frac{1}{\varrho_0 a\cos\Phi} \left(\cos\Phi \frac{\overline{v'\Theta'}}{\overline{\Theta}_z} \right)_\Phi \tag{5}$$

In these equations v and w are the meridional and vertical wind, respectively, Θ the potential temperature, and v' and Θ' perturbations of the meridional wind and potential temperature with respect to their zonal mean.

The zonal mean wave drag $\overline{X}_{res}$ of the waves that are explicitly resolved using the ERA analysis products (both global-scale and gravity waves) can be calculated from the divergence of the Eliassen-Palm flux (EP flux). The meridional ($\boldsymbol{F}^{(\Phi)}$) and the vertical component ($\boldsymbol{F}^{(z)}$) of the EP flux can be expressed as follows:

$$\boldsymbol{F}^{(\Phi)} = \varrho_0 a \cos\Phi \left(\frac{\overline{v'\Theta'}}{\overline{\Theta}_z} \overline{u}_z - \overline{u'v'} \right) \tag{6}$$

$$\boldsymbol{F}^{(z)} = \varrho_0 a \cos\Phi \left[\left(f - \frac{(\overline{u}\cos\Phi)_\Phi}{a\cos\Phi} \right) \frac{\overline{v'\Theta'}}{\overline{\Theta}_z} - \overline{u'w'} \right] \tag{7}$$

The EP flux divergence is given by

$$\nabla \cdot \boldsymbol{F} = \frac{1}{a\cos\Phi} \frac{\partial}{\partial\Phi} \left(\boldsymbol{F}^{(\Phi)} \cos\Phi \right) + \frac{\partial}{\partial z} \boldsymbol{F}^{(z)} \tag{8}$$

And the resolved wave drag is

$$\overline{X}_{res} = \frac{1}{\varrho_0 a \cos\Phi} \nabla \cdot \boldsymbol{F} \tag{9}$$

In the following, we will use $\overline{X}_{res}$ from ERA-Interim integrated over zonal wave numbers 1–20 as an estimate for the contribution of planetary waves $\overline{X}_{PW}$ in equation (3). The choice of this wave number range is somewhat arbitrary. In particular, the highest wave numbers will already be a mixture of planetary waves and resolved gravity waves, and the wave number range 1–20 will therefore probably result in an upper estimate for $\overline{X}_{PW}$. The contribution of even higher zonal wave numbers in ERA-Interim is very small and also not considered to be very reliable. Please note that in ECMWF operational data with even better longitudinal resolution than the 0.7° (T255) of ERA-Interim, the amplitudes of resolved gravity waves are generally much lower than in observations, and the global distribution of gravity waves in the tropics is not very realistic [e.g., *Schroeder et al.*, 2009].

Based on this estimate of $\overline{X}_{PW}$, we can calculate the wave drag that is missing in the ERA-Interim data set, and we can use this missing drag as an estimate for the drag $\overline{X}_{GW}$ that is expected to be contributed by gravity waves. This approach is similar to the one presented in *Alexander and Rosenlof* [2003] and relies on the assumption that the temperature and wind fields of the reanalysis are quasi-realistic by using a good underlying model, as well as the assimilation of a large number of observations in combination with good quality control and good analysis procedures.

2.3.2. Discussion of Results

The zonal wind in m/s and the different terms of the tropical momentum budget (see equation (3)) in m/s/d, averaged over the latitude band 10°S–10°N are displayed in Figure 1. To match with the time intervals used for the gravity wave analysis of HIRDLS and SABER data (see section 2.2.2), all values are averages over 7 days with a time step of 3 days (i.e., represent overlapping time windows). Shown are the zonal wind in m/s (Figure 1a), the zonal wind tendency $\partial\overline{u}/\partial t$ (Figure 1b), the meridional advection term $\overline{v}^* \left(\left(\overline{u}\cos\Phi\right)_\Phi / (a\cos\Phi) - f \right)$ (Figure 1c), the vertical advection term $\overline{w}^* \overline{u}_z$ (Figure 1d), the resolved wave drag $\overline{X}_{PW}$ for zonal wave numbers 1–20 (Figure 1e), and the residual term $\overline{X}_{GW}$ (Figure 1f) representing the missing drag attributed to gravity waves. This "missing drag" comprises the small contribution of explicitly resolved waves in ERA-Interim with zonal wave numbers >20, as well as parameterized gravity wave drag and the imbalances of the ERA-Interim momentum budget that are caused by data assimilation. Values of the zonal mean zonal wind are overplotted as contour lines in Figure 1.

Figure 1a shows the alternating pattern of QBO eastward and westward winds. During QBO phases of westward directed wind, the wind speed is considerably stronger (about −40 m/s) than during QBO eastward wind phases (about 20 m/s). As mentioned before, the phases of eastward and westward zonal wind descend with time, which is indicative for a wave-driven change of circulation. The vertical extent of QBO

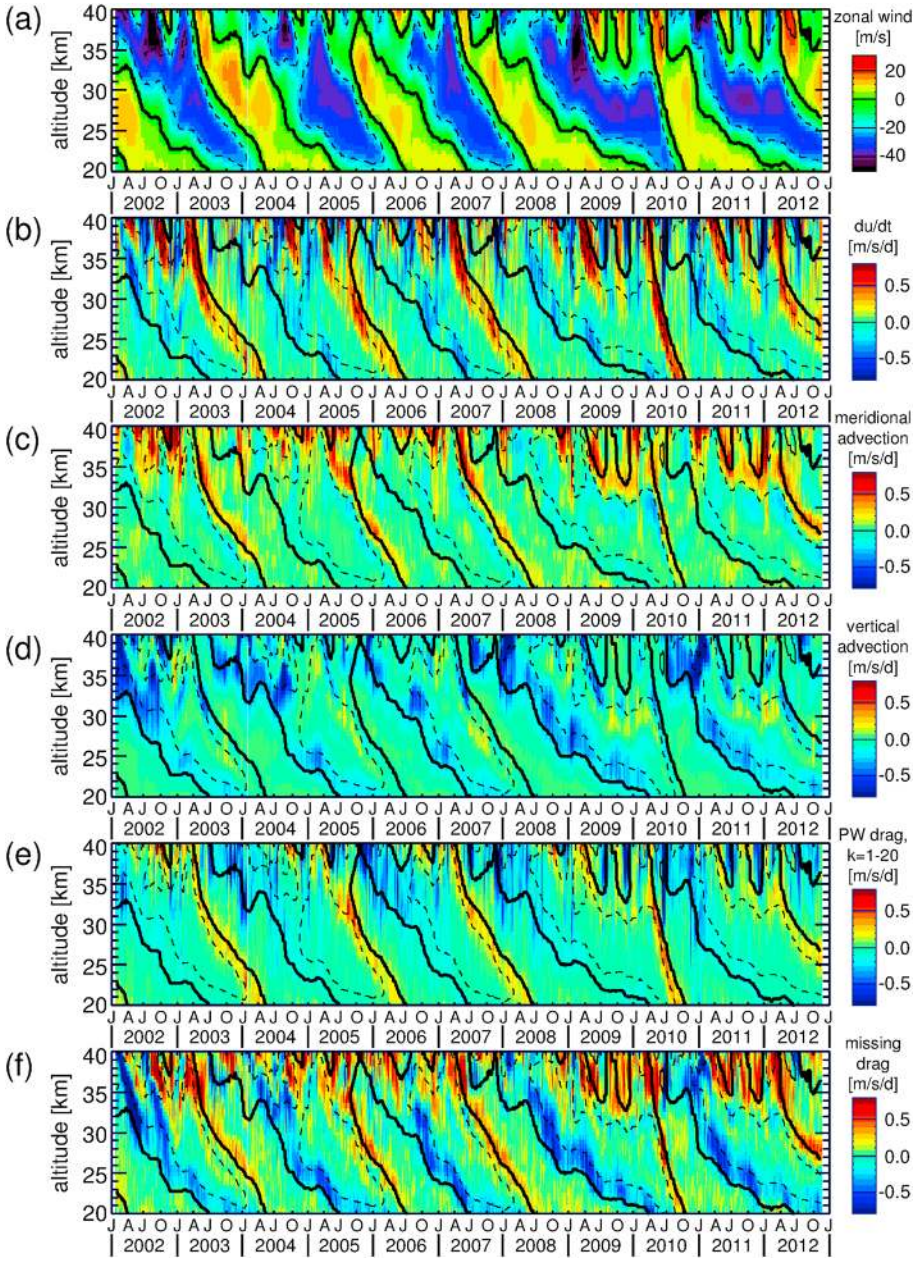

Figure 1. Altitude-time cross sections of the 10°S–10°N average (a) ERA-Interim zonal wind in m/s, and the following terms of the ERA-Interim tropical momentum budget in m/s/d: (b) zonal wind tendency $\partial\overline{u}/\partial t$, (c) meridional advection term, (d) vertical advection term, (e) planetary wave drag from EP flux divergence including zonal wave numbers 1–20, and (f) missing drag that is attributed to gravity waves. Figure 1f is the sum of Figures 1b, 1c, and 1d minus Figure 1e. Contour lines represent the zonal wind from Figure 1a. The bold solid line is the zero wind line. Dashed (solid) lines indicate westward (eastward) wind. Contour interval is 20 m/s.

westward and eastward phases varies considerably. Sometimes the QBO wind bands are as narrow as only about 5 km. Of course, this narrow vertical extent of the QBO wind bands requires high vertical resolution of the gravity wave analysis and, accordingly, a small vertical analysis window. We therefore mainly use high-pass filtered HIRDLS and SABER data (containing only vertical wavelengths <12 km) and a 5 km vertical window to obtain an altitude resolution as fine as possible (see also section 2.2.2). The analysis described in *Ern et al.* [2011] that is based on a coarser 10 km vertical window is only used for the determination of gravity wave spectra (see Appendix B).

The zonal wind tendency (Figure 1b) reaches values as high as 1 m/s/d for periods of strong QBO-related eastward wind shear. For westward wind shear the tendency is considerably weaker and rarely exceeds values of −0.5 m/s/d. The meridional advection term (Figure 1c) is usually weaker than 0.2 m/s/d but can attain values as large as 0.5 m/s/d around the zero wind lines during eastward wind shear of the QBO. The vertical advection term (Figure 1d) is usually weak (below 0.2 m/s/d), but at the beginning of the QBO westward wind phases it sometimes can attain values as strong as −0.5 m/s/d.

The most robust term of the different tendency terms discussed so far is probably the zonal wind tendency because this term is relatively large and directly related to the winds assimilated from observations, at least in the lower and middle stratosphere. The terms shown in Figures 1c and 1d, however, include the relatively weak residual circulation terms $\overline{v}^*$ and $\overline{w}^*$ and will therefore be more uncertain.

The drag due to resolved waves $\overline{X}_{PW}$ (Figure 1e) usually is strongest around the zero wind lines with the more well-defined maxima during eastward wind shear of the QBO. Peak values usually are around 0.3 m/s/d but sometimes can be as high as 0.5 m/s/d. During westward wind shear in the lower stratosphere values usually are weaker than 0.2 m/s/d. Only in the middle and upper stratosphere, values sometimes can be as strong as −0.5 m/s/d. The resolved wave drag is only as reliable as the global-scale waves in ERA-Interim are reliable, which is likely the case in the lower stratosphere [e.g., *Ern et al.*, 2008], but might no longer hold in the upper stratosphere and above [see also *Ern et al.*, 2009b].

The residual term $\overline{X}_{GW}$, which represents the missing drag due to gravity waves, is obtained from all the other terms (see equation (3)) and therefore is the most uncertain term of all. Values reach about 0.5 m/s/d during eastward wind shear of the QBO and about −0.5 m/s/d during westward wind shear. During westward wind shear the strongest values coincide with the values of the strongest wind shear. However, during the periods of QBO eastward wind shear, maximum values are attained at altitudes somewhat above the strongest wind shear, i.e., maxima of the missing drag are found at somewhat higher altitudes than the maxima of planetary wave drag. Similar behavior has been found for the gravity wave drag in several model simulations of the QBO [e.g., *Giorgetta et al.*, 2006; *Kawatani et al.*, 2010; *Evan et al.*, 2012], which supports our assumption that the missing drag in ERA-Interim can indeed be attributed to gravity waves. The maximization of planetary wave drag slightly before (i.e., below) the zero wind lines is also qualitatively in good agreement with observations of Kelvin wave drag during eastward wind shear [e.g., *Ern and Preusse*, 2009a, 2009b].

The missing drag $\overline{X}_{GW}$ is usually somewhat stronger than $\overline{X}_{PW}$ during eastward wind shear of the QBO and considerably stronger during westward wind shear. This shows that gravity waves are very likely more important for the driving of the QBO than global-scale waves, in particular during westward wind shear. Our results for $\overline{X}_{GW}$ are also in reasonable agreement with a similar analysis by *Monier and Weare* [2011] based on ERA-40 data. In *Monier and Weare* [2011] peak values of missing drag are about ±0.4 m/s/d.

3. QBO-Related Variation of the Observed Gravity Wave Distribution

3.1. Gravity Wave Variances

First, we investigate how gravity wave temperature variances that are observed by HIRDLS and SABER are modulated by the QBO. In order to preserve the full altitude resolution of the satellite instruments, Figures 2a–2d show the gravity wave temperature variances obtained directly after removing the global-scale waves. Figures 2a and 2b show SABER and HIRDLS temperature variances averaged over the latitude band 10°S–10°N for vertical wavelengths <25 km [see also *Ern et al.*, 2011]. Figures 2c and 2d show the same but with an additional FFT high-pass filter applied so that only vertical wavelengths <12 km are still contained in the data.

The observed gravity wave variances in the tropics show a very characteristic pattern with enhancements directly below the QBO zero wind lines. This is seen in all panels of Figure 2. This finding can be explained by the following theoretical considerations: Close to the critical level (before saturation occurs) the amplitude growth of a gravity wave is proportional to $|\overline{u} - c|^{-1/2}$ [see *Lindzen*, 1981; *Randel and Wu*, 2005, Appendix A], with $\overline{u}$ the zonal mean zonal wind and c the ground-based phase speed of the gravity wave. On the other hand, the critical amplitude limit for the onset of wave breaking is proportional to $|\overline{u} - c|$ [see *Ern et al.*, 2008, equation (10)]. Therefore, if in strong vertical wind shear $|\overline{u} - c|$ tends to 0, an increase of the wave variance proportional to $|\overline{u} - c|^{-1}$ would be expected until saturation is reached. Then, after reaching saturation, the

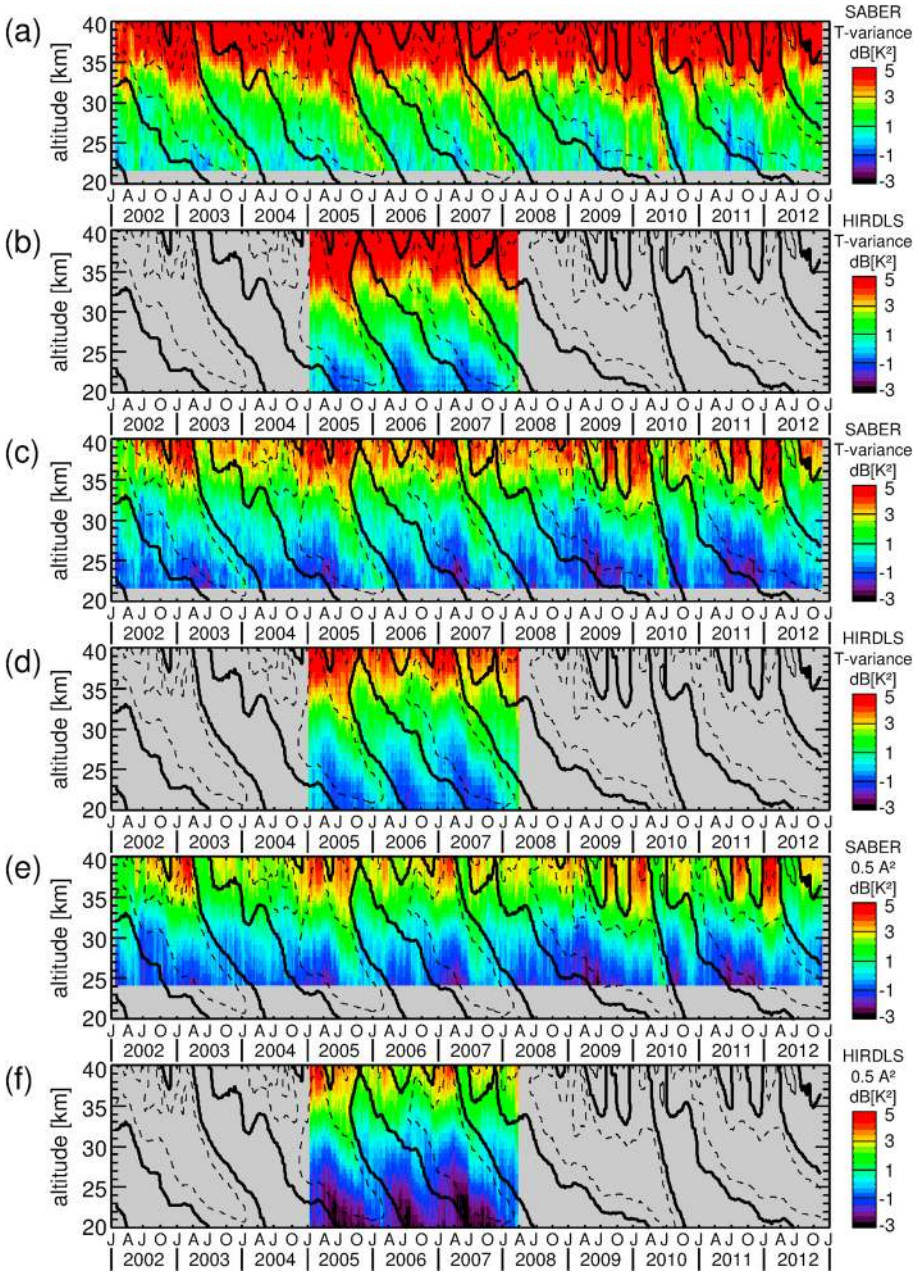

Figure 2. Altitude-time cross sections of (a) SABER gravity wave temperature variances, averaged over 10°S–10°N. Different from gravity wave amplitude estimates, no vertical window was applied. (b) Same as Figure 2a but for HIRDLS. (c, d) Same as Figures 2a and 2b but with a vertical wave number high-pass (cutoff at λ_z=12 km) applied to the SABER and HIRDLS temperature altitude profiles. (e) Average gravity wave squared amplitudes determined in 5 km vertical windows for the high-passed SABER altitude profiles. Values were divided by 2 to be comparable to the variances in Figures 2a–2d. (f) Same as Figure 2e but for HIRDLS. Units in Figures 2a–2f are dB(K^2). Contour lines indicate the zonal wind: westward wind is dashed, and the bold contour line indicates zero wind. Contour increment is 20 m/s.

variance is expected to decrease proportional to $|\overline{u} - c|^2$. A combination of these two effects would result in a variance maximum somewhat below the critical wind line.

Close to the QBO zero wind lines for a large part of the whole spectrum of gravity waves, the critical levels (i.e., $\overline{u} - c = 0$) nearly coincide. This probably leads to the observed layers of enhanced gravity wave variances. In particular, because the QBO eastward wind shear is much stronger than the westward wind shear, this enhancement of gravity wave variances should be more pronounced for the eastward wind shear

phases of the QBO—simply because a larger part of the wave spectrum reaches its critical wind level at almost the same altitude [see also *Ern et al.*, 2013a].

This theoretical behavior is also qualitatively found in the observations: in Figures 2a and 2b between 20 and 30 km altitude, peak values of gravity wave variances during eastward wind shear are about 3.5 dB (∼2.3 K^2) and are about 2 dB (∼1.6 K^2) during westward wind shear. Minimum variances are about −1 dB (∼0.8 K^2). These values are about the same for both SABER and HIRDLS, only sometimes HIRDLS is ∼0.5 dB lower than SABER. The reason for this minor difference of about 12% is unknown. In the high-pass filtered data sets (Figures 2c and 2d) the QBO-related variations of gravity wave variances are perhaps even more characteristic. Between 20 and 30 km altitude, peak values of variances during QBO eastward wind shear are about 2 dB (∼1.6 K^2) and are about 0.5 dB (∼1.1 K^2) during westward wind shear. Minimum variances are about −2 dB (∼0.6 K^2). Again, we find good agreement between SABER and HIRDLS.

Figures 2e and 2f show SABER and HIRDLS gravity wave squared amplitudes. Values were divided by 2 to match the variances shown above. These amplitudes represent the strongest waves obtained from a windowed vertical analysis of altitude profiles as described in *Preusse et al.* [2002] and *Ern et al.* [2004]. This method was applied with a 5 km vertical window to the high-pass filtered SABER and HIRDLS data containing only waves with vertical wavelengths <12 km. Again, there is good agreement between HIRDLS and SABER, and the relative variations seen in Figures 2e and 2f are qualitatively the same as in Figures 2c and 2d. However, values of the squared amplitudes divided by 2 are generally about 1 dB (about 30%) lower than the variances shown in Figures 2c and 2d. This small reduction of squared amplitudes divided by 2 with respect to the variances is partly due to the vertical averaging effect of the 5 km vertical analysis window. And, of course, some of the variance is also carried by weaker waves that may be present in a given altitude profile at a given altitude, in addition to the dominant wave. These weaker waves are not contained in the squared amplitudes shown in Figures 2e and 2f, and they are also neglected for the momentum flux calculation. Further, the averaging effect of the vertical window also reduces the effect of noise contained in the measurements. This effect is particularly important at low altitudes, where gravity wave amplitudes are low.

The squared amplitudes shown in Figures 2e and 2f were determined from single altitude profiles. The average squared amplitudes that are obtained for pairs of altitude profiles are almost exactly the same and are therefore not shown. Most importantly, the analysis based on the narrow 5 km vertical window is obviously capable of resolving the vertical variations of the gravity wave distribution, which is a precondition for obtaining meaningful results in our further analyses (see below). Overall, the relative variations of temperature variances and squared amplitudes in Figure 2 are very similar, and the location of the maxima directly below the zero wind lines indicates that critical level filtering of gravity waves is important in the whole altitude range considered.

Even though the largest part of the QBO-related variation is still contained in the high-pass filtered data set, we have to make sure that not much of the relevant part of the momentum flux spectrum and its vertical variations are missed. As detailed below, this should not be the case, because mainly gravity waves that have intrinsic phase speeds smaller than the maximum wind below the wind reversal should dissipate during this wind reversal.

In midfrequency approximation the dispersion relation for gravity waves is

$$\hat{\omega} = N k_h / m \tag{10}$$

with $\hat{\omega}$ the intrinsic frequency, N the buoyancy frequency, k_h the horizontal, and m the vertical wave number [e.g., *Fritts and Alexander*, 2003]. The intrinsic phase speed $\hat{c}$ of the wave is given by

$$\hat{c} = \hat{\omega}/k_h = N/m = \lambda_z N/(2\pi) \tag{11}$$

and (for midfrequency gravity waves) depends only on the vertical wavelength λ_z of the wave and the buoyancy frequency. Assuming a value of $N = 0.02\,s^{-1}$, which is a good approximation in the stratosphere, a vertical wavelength of 12 km corresponds to an intrinsic phase speed of $\hat{c} = 40$ m/s. This is about the maximum QBO wind that is observed. This means that mainly gravity waves having vertical wavelengths <12 km below the wind reversal will encounter critical wind levels during the wind reversal. From these theoretical considerations, in order to capture the largest part of the gravity wave driving of the QBO it should be sufficient to investigate the high-pass filtered SABER and HIRDLS data sets containing only gravity waves

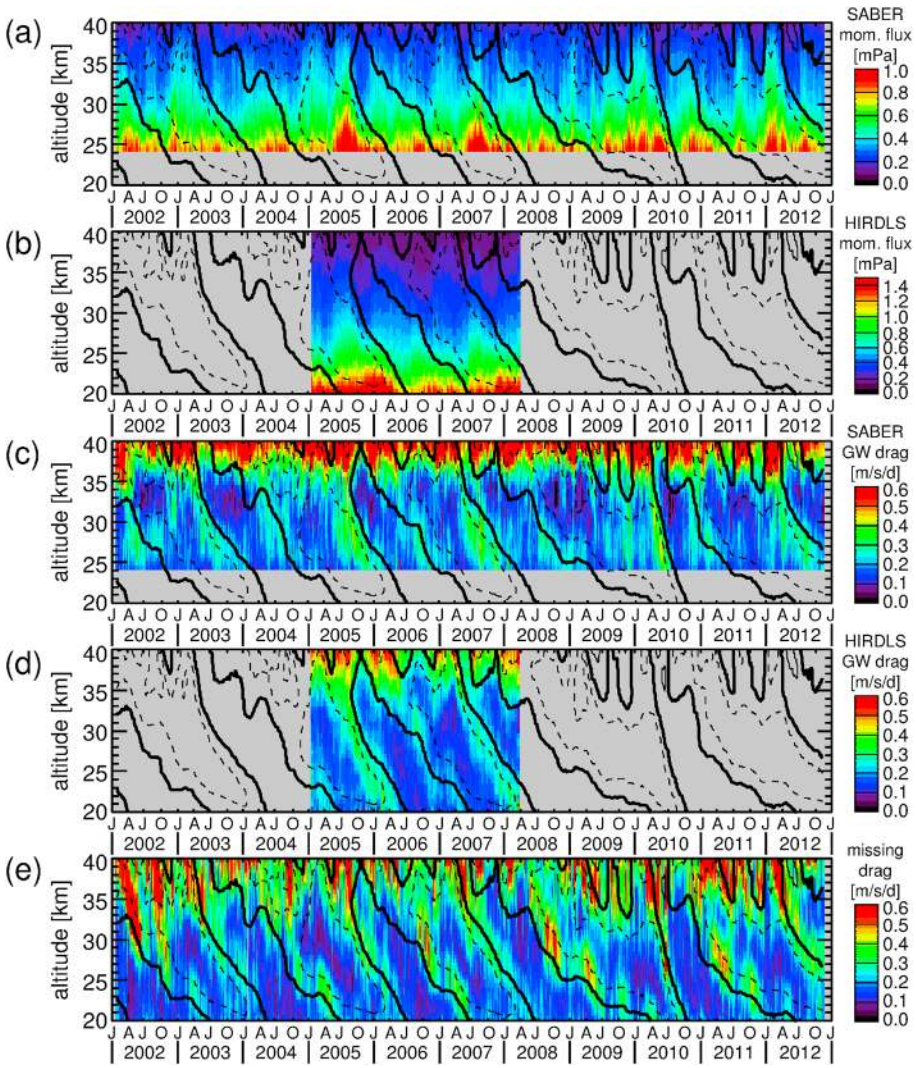

Figure 3. Altitude-time cross sections of (a) 10°S–10°N average SABER total gravity wave momentum fluxes from a gravity wave analysis using a 5 km vertical window and a data set containing only vertical wavelengths <12 km. (b) Same as Figure 3a but for the HIRDLS instrument. (c and d) Total gravity wave drag obtained from vertical gradients of the SABER and HIRDLS momentum fluxes shown in Figures 3a and 3b, respectively. (e) Absolute values of the missing zonal wave drag in ERA-Interim, smoothed with a 5 km vertical running mean.

with λ_z <12 km. This is further confirmed by the gravity wave momentum flux spectra shown in Appendix B. From these spectra it is clearly seen that the main reduction of gravity wave momentum fluxes due to QBO wind shear is at short vertical wavelengths (<12 km), which is as expected for critical level filtering of gravity waves.

3.2. Gravity Wave Total Momentum Flux and Drag

In the following, the variations of the total (absolute) momentum fluxes are studied. Again, we use the high-pass filtered data set of SABER and HIRDLS gravity wave temperature fluctuations containing only vertical wavelengths <12 km. All values are obtained from a momentum flux analysis using a 5 km vertical window, and they represent averages over the latitude band 10°S–10°N.

Figure 3a shows absolute momentum fluxes on a linear scale in 10^{-3} Pa for SABER and Figure 3b for HIRDLS. Please note that the scales in 3a and 3b are different because our SABER data start at higher altitudes and therefore cover a smaller range of momentum fluxes. Both SABER and HIRDLS momentum fluxes show a general decrease with altitude. At low altitudes, close to the sources of the gravity waves, momentum flux is high. Without wave dissipation taking effect, momentum flux would be a conserved quantity. The observed decrease of momentum flux with altitude indicates that there is wave dissipation throughout the

stratosphere. It is remarkable that the distribution of momentum fluxes in Figures 3a and 3b shows a characteristic sawtooth-like shape that is closely related to the zonal wind shear and zero wind lines of the QBO. This sawtooth-like (triangular) structure is caused by critical level filtering of parts of the wave spectrum and indicates that wave driving contributes to the observed wind reversals. Similar behavior has been found for the dissipation of Kelvin waves during the QBO wind reversal from westward to eastward winds [*Ern and Preusse*, 2009a] and for the dissipation of gravity waves during the reversal of the mesospheric wind jets from summertime westward to wintertime eastward winds [*Ern et al.*, 2013b]. Regardless of the coarser horizontal sampling of SABER and the limitation to vertical wavelengths longer than 4–5 km, we again find remarkable agreement between the SABER and HIRDLS momentum fluxes, both in the relative distribution and in the magnitudes.

In Figures 3c and 3d the total gravity wave drag derived from vertical gradients of the total (absolute) momentum fluxes is shown for SABER and HIRDLS, respectively. We find enhanced values of gravity wave drag always during periods of strong QBO wind shear (both eastward and westward). Maximum values are about 0.3 m/s/d for the eastward to westward QBO wind reversals, and about 0.4 m/s/d for the westward to eastward wind reversals. The somewhat higher values during the westward to eastward wind reversals are qualitatively in good agreement with the fact that the eastward wind shear usually is stronger than the westward wind shear. HIRDLS and SABER values of maximum drag are comparable, but HIRDLS drag values are somewhat weaker. Overall, the HIRDLS gravity wave drag distribution is less noisy and less smeared out than the SABER distribution. One possible reason might be the better altitude resolution of HIRDLS that allows it to detect gravity waves even close to their dissipation altitudes where they attain very short vertical wavelengths, which then produces sharper maxima of gravity wave drag. Further, owing to the much denser sampling, HIRDLS has a much better statistics (more observations) which may help to reduce noise. This noise may arise from both the instrument and the strongly intermittent nature of gravity wave activity. Apart from these minor differences, the overall agreement between SABER and HIRDLS is remarkably good.

For a better comparison with the ERA-Interim missing drag (see section 2.3), absolute values of ERA-Interim missing drag have been calculated from the 7 day average values of the different ERA-Interim momentum budget terms latitude by latitude. Then these missing drag values were averaged over the latitude band 10°S–10°N and smoothed vertically by a 5 km running mean. The result is shown in Figure 3e. In this way we account for the fact that SABER and HIRDLS drag are only total (absolute) drag and that for SABER and HIRDLS an analysis with a 5 km vertical window was used. Please note that by first taking the absolute values of the ERA-Interim missing drag and averaging afterward over the different latitudes, somewhat higher values are obtained as would be the case if simply taking the absolute value of the missing drag shown in Figure 1f. This is the case because some cancellation of positive and negative ERA-Interim missing drag at different latitudes is avoided, which might be more realistic when comparing to the observed total drag values from HIRDLS and SABER.

There is a remarkable overall agreement between the gravity wave drag distributions derived from satellite observations (Figures 3c and 3d) and the absolute ERA-Interim missing drag (Figure 3e), even in many details. For example, it is found in all three data sets that gravity wave drag obviously acts more continuously during the QBO westward to eastward wind reversals. During QBO eastward to westward wind reversals, however, gravity wave drag occurs more in a series of bursts. This is also reflected in the more stepwise descent of the zero wind lines in altitude during QBO westward wind shear.

There are also some important differences between observed gravity wave drag and ERA-Interim missing drag. For example, there is a shift in altitude between the patterns of observed and ERA-Interim missing drag. Maxima of ERA-Interim drag are found usually at altitudes about 1 km above the observed drag, in particular during QBO eastward wind shear. One possible reason for this effect could be uncertainties in the different momentum budget terms in ERA-Interim. These uncertainties would also affect the missing drag, which relies on the accuracy of all the other momentum budget terms. Another reason could be observational filter effects of the satellite instruments. Due to the vertical field of view of the instruments, HIRDLS cannot detect gravity waves with vertical wavelengths shorter than 2 km, and SABER can only detect gravity waves with vertical wavelengths longer than 4–5 km. When gravity waves are close to their dissipation altitude, their vertical wavelength can be very short and therefore are no longer detectable for HIRDLS and SABER. This effect shifts the observed momentum flux vertical gradients and the resulting gravity wave drag toward lower altitudes. In Figures 4 and 5 a vertical shift of 1 km is assumed (see sections 3.3.1 and 3.3.2).

The altitudes of HIRDLS and SABER peak gravity wave drag match the altitudes of peak ERA-Interim zonal wind tendencies $\partial\overline{u}/\partial t$ (see Figure 1b) somewhat better than the altitudes of peak ERA-Interim missing drag (Figure 3e). However, in QBO model simulations, peak values of gravity wave drag are often located about 1 km above the peak values of $\partial\overline{u}/\partial t$, in particular during eastward wind shear (see, for example, *Giorgetta et al.* [2006, Figure 10] and *Evan et al.* [2012, Figure 10]). This is in good qualitative agreement with the altitude shift between peak values of $\partial\overline{u}/\partial t$ and the missing drag in ERA-Interim. Therefore, limitations in the observational filters of the HIRDLS and SABER instruments are the more likely reason for the small altitude shift between observed gravity wave drag and ERA-Interim missing drag.

Another difference between HIRDLS and SABER drag and the absolute missing drag in ERA-Interim are details in the gravity wave drag absolute values. ERA-Interim peak values during QBO eastward wind shear are about 0.4 m/s/d, i.e., similar to the peak values of the HIRDLS and SABER drag. During QBO westward wind shear, however, ERA-Interim peak values are about 0.6 m/s/d, i.e., higher than during QBO eastward wind shear. This is in contrast to the HIRDLS and SABER peak drag during QBO westward wind shear, which is only about 0.3 m/s/d, i.e., weaker than during QBO eastward wind shear.

Of course, the spectrum of gravity waves contributing to the QBO westward wind shear could be different from the spectrum during eastward wind shear, so that HIRDLS and SABER might observe only a smaller fraction of the gravity wave drag during QBO westward wind shear. Another explanation could be uncertainties in the ERA-Interim momentum budget. The westward drag in ERA-Interim is mainly due to the contribution of the vertical advection term in equation (3) (see also Figure 1d). Therefore, this could indicate either that the vertical velocity $\overline{w}^*$ might be too strong in ERA-Interim or that the wave drag of westward propagating planetary waves is underestimated.

It is also remarkable that the part of the gravity wave spectrum that is observed by HIRDLS and SABER alone can explain much of the missing drag in ERA-Interim, particularly during QBO eastward wind shear. This could be a hint that the short horizontal wavelength part of the gravity wave spectrum that is not visible for HIRDLS and SABER (λ_h <100 km) does not contribute much. This could happen if the gravity waves with λ_h <100 km generally have phase speeds >40 m/s at their source level, or if they dissipate mainly at higher altitudes. Other possibilities could be uncertainties in the HIRDLS and SABER gravity wave drag (see also section 2.2), or the missing drag in ERA-Interim might be underestimated for some reason.

These findings show the importance in investigating the gravity wave spectrum at horizontal wavelengths λ_h <100 km in more detail. This problem has already been recognized before when simulated spectra of convectively generated gravity waves were compared to observations [e.g., *Choi et al.*, 2012]. Further, the resolved waves and the vertical velocity $\overline{w}^*$ in ERA-Interim should be validated by comparison to observations. This is, however, beyond the scope of our current study.

3.3. Gravity Wave Contribution to the QBO: A More Quantitative Approach

3.3.1. Time Series at 30 km Altitude

To allow a more quantitative comparison between the observed HIRDLS and SABER gravity wave drag and the ERA-Interim missing drag, we now investigate the time series at 30 km altitude, about the center altitude of the QBO in the tropics. Again, all shown parameters represent zonal averages of 6-hourly data, averaged over 7 days and the latitude band 10°S–10°N. The time step of the data series is 3 days. Figure 4a shows the zonal wind from ERA-Interim in m/s at 30 km altitude. Times of zero zonal wind at 30 km are indicated as brown vertical lines in all panels of Figure 4. Periods of strong westward (eastward) wind shear are marked by gray (orange) shading.

In Figure 4b the different terms of the ERA-Interim momentum budget are compared. Shown are the zonal wind tendency $\partial\overline{u}/\partial t$ (black curve), the sum of meridional and vertical advection terms (blue curve), the drag due to resolved planetary waves with zonal wave numbers 1–20 (green curve), and the missing drag that is attributed to gravity waves (red curve). The sum of black and blue curves is equal to the sum of the green and red curves. For better display, the curves in Figure 4b were smoothed by a nine-point running mean (i.e., 27 days). Beneath the QBO-related variations that have already been discussed in section 2.3.2, there are several important findings: The different tendency terms are often of the same size, showing that the momentum budget of the QBO is very complicated. The drag of planetary waves always explains part of $\partial\overline{u}/\partial t$ and is occasionally very strong during QBO eastward wind shear. It is also evident that the advection terms play a very important role. During westward wind shear they have the same direction as $\partial\overline{u}/\partial t$ and can be very strong even if $\partial\overline{u}/\partial t$ itself is very weak. These strong values are balanced by very high values of

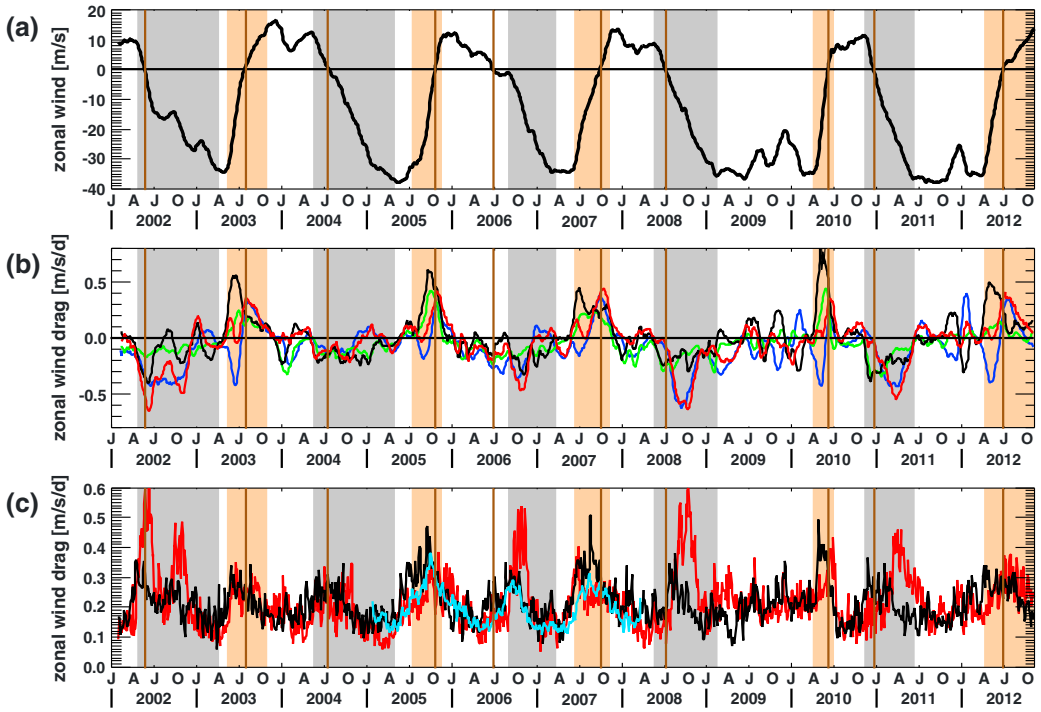

Figure 4. Zonal momentum balance for the QBO at 30 km altitude for the time period 2002–2012. All parameters are averages over the latitude band 10°S–10°N. (a) Zonal average zonal wind from ERA-Interim in m/s. (b) ERA-Interim momentum budget with the contributions (black) $\partial\overline{u}/\partial t$, (blue) sum of vertical and meridional advection terms, (green) resolved waves with zonal wave numbers 1–20 (planetary waves), and (red) missing drag attributed to gravity waves. (c) Comparison of the absolute ERA-Interim missing drag at 30 km altitude averaged vertically over 5 km (red curve) and the observed gravity wave drag at 29 km from HIRDLS (light blue) and SABER (black). Periods of strong westward (eastward) wind shear are indicated by gray (orange) shading. Times when the zonal wind at 30 km is 0 are marked by brown vertical lines. The curves in Figure 4b are smoothed by a nine-point running mean (corresponding to 27 days) for better display.

missing drag, often exceeding $\partial\overline{u}/\partial t$. During QBO eastward wind shear, the advection terms partly counteract $\partial\overline{u}/\partial t$ (see also Figure 1). Together with the planetary wave drag this leads to values of missing drag that usually are somewhat lower than $\partial\overline{u}/\partial t$.

The red curve in Figure 4c shows absolute values of the missing drag in ERA-Interim, additionally smoothed vertically by a 5 km running mean (see also section 3.2), to allow a better comparison with the HIRDLS (light blue curve) and SABER (black curve) total observed gravity wave drag. To account for the vertical shift in the drag patterns that was discussed before, we compare the absolute ERA-Interim missing drag at 30 km altitude with the HIRDLS and SABER gravity wave drag from 29 km. There is very good agreement between SABER and HIRDLS, and also the temporal variations of absolute ERA-Interim missing drag and observed drag correspond very well. During QBO eastward wind shear, even absolute values are in good agreement. Only during QBO westward wind shear, the ERA-Interim missing drag is often considerably stronger. Because HIRDLS and SABER only observe part of the gravity wave spectrum, we expect the observed drag to be weaker than the ERA-Interim missing drag for both eastward and westward QBO wind shear. Since this is not the case, this imbalance between observations and ERA-Interim missing drag might hint at uncertainties in the advection terms of the momentum budget: the advection terms are very strong during westward wind shear (even though $\partial\overline{u}/\partial t$ itself may be weak), and they partly counteract the wind tendency during QBO eastward wind shear. It is also remarkable that the noise-like short-term variability (intermittency) of ERA-Interim missing drag is stronger than for the HIRDLS gravity wave drag. This short-term variability on time scales shorter than 1 month is also present in the single terms of the ERA-Interim momentum budget but does not show in Figure 4b because the curves in Figure 4b were smoothed.

3.3.2. Average Altitude Profiles

In Figure 5 we investigate the vertical variation of the different QBO momentum budget terms, averaged separately for QBO eastward and westward wind shear over all available periods of zonal wind weaker than 5 m/s at 28 km altitude. Please note that the time coverage is different for the three data sets used (SABER and ERA-Interim about 11 years, and HIRDLS about 3 years). The 28 km altitude level was selected for comparison with Figure 10 in *Giorgetta et al.* [2006].

For the case of QBO eastward zonal wind shear at 28 km altitude, Figure 5a shows altitude profiles of the ERA-Interim QBO zonal wind (black dashed curve), the zonal wind tendency $\partial\overline{u}/\partial t$ (black curve), the sum of meridional and vertical advection terms (blue curve), the drag due to resolved planetary waves with zonal wave numbers 1–20 (green curve), and the missing drag that is attributed to gravity waves (red curve). Both $\partial\overline{u}/\partial t$ and the planetary wave drag peak somewhat below the zero wind altitude of 28 km. Different from this, the drag due to the advection terms peaks somewhat above the zero wind altitude. Close to the zero wind altitude, the missing drag is dominated by the advection terms and therefore also the missing drag peaks above the zero wind altitude (see also section 2.3.2). During westward wind shear (Figure 5c) the situation is very similar. Only the vertical extent of the drag maxima is larger (about 10 km instead of about 5 km) because the wind shear also extends over a larger altitude range. It should, however, be mentioned that the details of this comparison strongly depend on the choice of the zero wind altitude. For example, for other choices of zero wind altitudes there is not so close agreement between $\partial\overline{u}/\partial t$ and planetary wave drag or between advective and missing drag.

Figures 5b and 5d show comparisons between HIRDLS and SABER total gravity wave drag (light blue and black curves, respectively) and the ERA-Interim absolute missing drag (red curve) and zonal wave number 1–20 planetary wave absolute drag (green curve), both smoothed vertically by a 5 km running mean (see also section 2.3.2). SABER and HIRDLS total drag are shifted by 1 km toward higher altitudes for better comparison (see also section 3.3.1).

During QBO eastward wind shear, qualitatively good agreement between HIRDLS and SABER total drag and ERA-Interim absolute missing drag is found: there is a maximum centered at about the zero wind altitude, a minimum at about 35 km, and an increase of drag at higher altitudes. The planetary wave drag shows a similar behavior. However, in the lower stratosphere planetary wave drag is weaker, and at higher altitudes somewhat stronger. There are also some differences between absolute ERA-Interim missing drag and HIRDLS and SABER gravity wave drag. For example, in the lower stratosphere HIRDLS drag is stronger than the ERA-Interim missing drag. This is even more the case for lower zero wind altitudes, which is also indicated in Figure 3 (see section 3.2). Another difference is that the minimum at 35 km altitude is somewhat deeper in HIRDLS and SABER gravity wave drag than in the ERA-Interim absolute missing drag. At this altitude the missing drag shown in Figure 5a is very low (<0.1 m/s/d), while the absolute missing drag in Figure 5b is somewhat stronger (about 0.2 m/s/d). This effect is even more pronounced for westward QBO wind shear (Figures 5c and 5d) and also found for the ERA-Interim planetary wave drag. A possible explanation is the cancellation of positive and negative drag values at different latitudes, resulting in lower net drag in Figures 5a and 5c. Whether these cancellation effects are realistic cannot be decided easily, and an investigation of meridional variations in the different zonal momentum terms is beyond the scope of our current study. Apart from this difference, during QBO westward wind shear (Figure 5d), the agreement between HIRDLS and SABER gravity wave drag and ERA-Interim absolute missing drag is very good in the lower stratosphere. However, it should again be noted that there are considerable differences in details, depending on the choice of the zero wind altitude.

In the following, we compare Figure 5 to results obtained in recent model simulations of the QBO, for example, the simulations by *Giorgetta et al.* [2006], *Evan et al.* [2012], or *Kawatani et al.* [2010]. Qualitatively, all these studies are in good agreement with our results. However, there are also important differences in details of the different forcing terms.

For example, in the study by *Giorgetta et al.* [2006] the value of peak gravity wave drag during QBO eastward wind shear is only 0.2 m/s/d, lower than their peak drag due to resolved waves (about 0.3 m/s/d). Different from this, in our study both observed gravity wave drag and the missing drag in ERA-Interim can reach values as high as 0.4 m/s/d. Also, the drag due to resolved waves in ERA-Interim is somewhat higher (about 0.4 m/s/d). During QBO westward wind shear, peak gravity wave drag values in *Giorgetta et al.* [2006] are

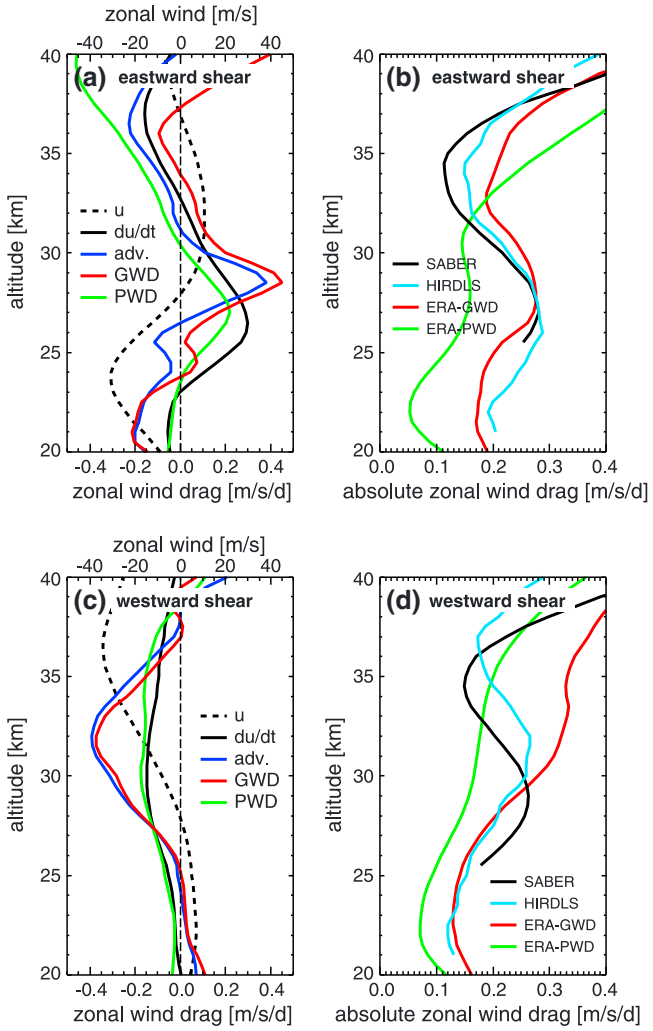

Figure 5. Altitude profiles of the different QBO momentum budget terms during (a and b) eastward wind shear as well as (c and d) westward wind shear at 28 km altitude. All values are averages over 10°S–10°N and over all available time periods of about zero wind at 28 km altitude. Figure 5a shows for QBO eastward wind shear at 28 km the zonal average zonal wind from ERA-Interim in m/s (black dashed, scale at upper *x* axis), as well as the following ERA-Interim momentum budget terms in m/s/d (scale at lower *x* axis): (black) $\partial\overline{u}/\partial t$, (blue) sum of vertical and meridional advection terms, (green) resolved waves with zonal wave numbers 1–20 (planetary waves), and (red) missing drag attributed to gravity waves. Figure 5b shows comparison of the ERA-Interim missing drag absolute values (red curve) and planetary wave drag absolute values (green curve), both averaged vertically over 5 km, and the observed gravity wave drag from HIRDLS (light blue) and SABER (black), both shifted upward in altitude by 1 km. Figures 5c and 5d show the same as Figures 5a and 5b, respectively, but for QBO westward wind shear at 28 km.

around 0.4 m/s/d, i.e., between the peak drag in HIRDLS and SABER observations of about 0.3 m/s/d and peak values of around 0.6 m/s/d in ERA-Interim missing drag.

In the study by *Evan et al.* [2012] during QBO eastward wind shear, peak values of gravity wave drag are about 0.4 m/s/d, comparable to our values. During westward wind shear, however, peak values are weaker (about 0.2 m/s/d), i.e., lower than our values and the ones in *Giorgetta et al.* [2006]. In *Evan et al.* [2012] most gravity wave drag arises from waves with horizontal scales ≥1000 km. As they state in their study, the contribution of small-scale and high-frequency gravity waves is likely underestimated. This is supported by the gravity wave spectra shown in our Figure B1 (see Appendix B): the difference in HIRDLS momentum fluxes between upper and lower levels has its peak at horizontal wavelengths $\lambda_h < 1000$ km. Further, in the study by *Evan et al.* [2012] only 50% of the gravity wave drag is due to waves with vertical wavelengths $\lambda_z 1. < 10$ km, while in our study the gravity wave spectra in Figure B1 indicate that the main reduction of momentum fluxes is at vertical wavelengths $\lambda_z < 10$ km.

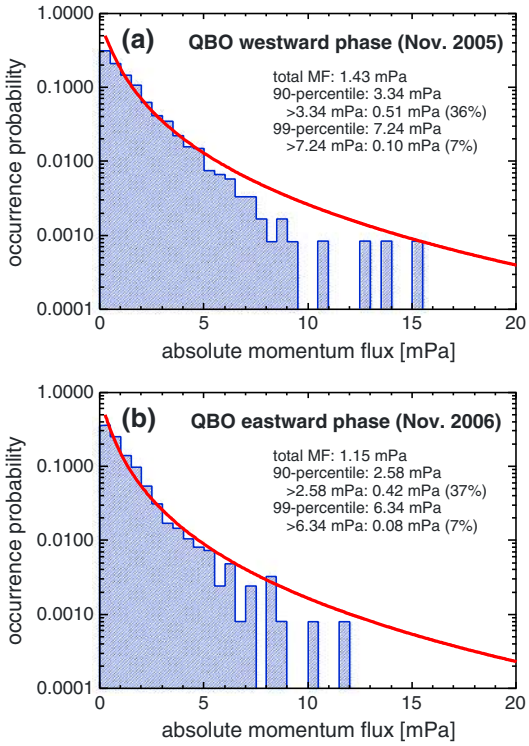

Figure 6. HIRDLS gravity wave momentum flux occurrence probability distribution at 20 km altitude in the latitude band 10°S–10°N during (a) QBO westward wind (November 2005) and (b) QBO eastward wind (November 2006). The red curves represent lognormal distributions with the same mean and standard deviation as the HIRDLS momentum fluxes.

In the study by *Kawatani et al.* [2010] at the pressure level 15 hPa (about 30 km altitude) peak values of gravity wave drag are as strong as 0.4 m/s/d, while global-scale waves with zonal wave numbers 1–11 have only weak drag of around 0.1 m/s/d at maximum. Also, the tendency terms due to the residual circulation are relatively weak, having peak values of only around 0.2 m/s/d. This means that the gravity wave drag in *Kawatani et al.* [2010] is comparable to our observed drag and the missing drag in ERA-Interim. Both the tendency terms due to the residual circulation and the drag due to global-scale waves are, however, somewhat weaker. Please note that in *Kawatani et al.* [2010] the peak values of gravity wave drag occur always later than the peak values in $\partial\overline{u}/\partial t$, which corresponds to the fact that the peaks of our ERA-Interim missing drag and of gravity wave drag in *Giorgetta et al.* [2006] and *Evan et al.* [2012] are at somewhat higher altitudes than the peak values in $\partial\overline{u}/\partial t$.

The comparison with these three studies shows that even if there is general agreement in the relative variations of the different forcing terms of the QBO momentum budget, there are still considerable uncertainties regarding their relative strength, as well as the spectrum of waves that contribute.

3.4. Intermittency of Observed Momentum Fluxes in the Tropics

Many parameterizations of gravity waves in GCMs and CCMs rely on uniform (constant) gravity wave source distributions. However, observations show that momentum fluxes of gravity waves in the real atmosphere are strongly intermittent (a mixture of strong and weak events) [e.g., *Hertzog et al.*, 2008, 2012]. Recently, it has been found that in GCMs/CCMs the generation of the QBO can be significantly improved by use of stochastic gravity wave source parameterizations [e.g., *Lott et al.*, 2012]. Therefore, observations of gravity wave intermittency in the tropics are important for comparison with those stochastic schemes in order to improve their parameter settings.

Since we are particularly interested in the intermittency of gravity waves close to their sources, we will investigate the intermittency of observed momentum fluxes at altitudes as low as possible. Further, we are mainly interested in the intermittency of the part of the wave spectrum that drives the QBO. Therefore, we again use the momentum fluxes obtained from high-pass filtered HIRDLS data containing only λ_z <12 km. The momentum fluxes should also not be affected by wind filtering of gravity waves during QBO wind reversals. We therefore focus on the months November 2005 and November 2006 and an altitude of 20 km. In this way we cover phases of both QBO westward (November 2005) and QBO eastward wind (November 2006). As before, we consider the latitude band 10°S–10°N.

The occurrence probability distribution of the observed absolute momentum fluxes is shown in Figure 6 for November 2005 (Figure 6a) and November 2006 (Figure 6b). The red curves represent lognormal distributions with the same mean and standard deviation as the observed momentum fluxes in the respective month [see also *Hertzog et al.*, 2012]. Different from the findings by *Hertzog et al.* [2012] for high southern latitudes during September and October 2005, in the tropics the observed momentum fluxes follow the lognormal distribution only for small and medium but not for the highest observed momentum fluxes. This means that the gravity wave sources in the tropics are less intermittent than in the southern polar vortex

where a large part of the momentum fluxes is from very intermittent mountain waves. (As a cross-check we have also reproduced the probability distributions in *Hertzog et al.* [2012] and find good agreement.)

Still, there is considerable intermittency of gravity waves in the tropics. In November 2005 (Figure 6a) only 10% of the momentum flux values are higher than 3.34 mPa, the 90th percentile value of the probability distribution. Nevertheless, these few values contribute as much as 36% to the average observed momentum flux of 1.43 mPa. The 99th percentile is 7.24 mPa, and momentum fluxes higher than this contribute as much as 7% to the total momentum flux. In November 2006 (Figure 6b) the total momentum flux is somewhat lower (about 1.15 mPa), but the intermittency of the observed waves is almost the same. Momentum fluxes exceeding the 90th percentile (99th percentile) contribute as much as 37% (7%) to the total momentum flux. These 90th percentile values in the tropics are qualitatively in good agreement with those of a recent study by *Wright et al.* [2013]. Our findings indicate that intermittency of gravity waves in the tropics could indeed play an important role, and simulations of the QBO in CCMs and GCMs might benefit from including this process.

4. Summary and Discussion

In our study we have used temperature observations of the satellite instruments High Resolution Dynamics Limb Sounder (HIRDLS) and Sounding of the Atmosphere using Broadband Emission Radiometry (SABER) to investigate the interaction of the global distribution of gravity waves (averaged over the latitude band 10°S–10°N) with the quasi-biennial oscillation (QBO) of the zonal wind in the tropics. Temperature fluctuations due to gravity waves have been determined by removing the contribution of global-scale waves from the observed temperature altitude profiles, following the procedure described in *Ern et al.* [2011, 2013b]. Beneath quasi-biennial variations that have been reported before [e.g., *Randel and Wu*, 2005; *de la Torre et al.*, 2006; *Krebsbach and Preusse*, 2007], our observed HIRDLS and SABER gravity wave variances also show a pronounced quasi-annual variation. Because gravity waves interact with the QBO during both eastward and westward wind shear, this additional quasi-annual variation is also what would be expected from theoretical considerations.

We have derived total (absolute) gravity wave momentum fluxes from HIRDLS and SABER residual temperatures using the method by *Ern et al.* [2004, 2011]. Gravity wave momentum flux spectra determined for both QBO eastward and westward wind shear show that during the QBO wind reversals the main change in the observed momentum fluxes is at vertical wavelengths <10 km. Therefore, we applied a vertical wave number high-pass filter to the residual temperatures and focused on the spectrum of gravity waves with vertical wavelengths <12 km. In this way the vertical resolution of the derived momentum fluxes could be improved from 10 to 5 km, which is required to resolve the narrow zonal wind bands of the QBO. For wave-driven wind reversals the regions of strong wind shear propagate downward with time. Because the dissipation and filtering of waves is closely connected with these shear zones, this downward propagation results in characteristic sawtooth-like (triangular) variations in altitude-time cross sections of momentum flux distributions [see also *Ern and Preusse*, 2009a; *Ern et al.*, 2013b]. Similar behavior was also found in our study for QBO-related variations of gravity wave momentum fluxes. The main reduction of gravity wave momentum flux was found for intrinsic phase speeds <30 m/s. This indicates that critical level filtering should be the main QBO-related dissipation process of gravity waves

Values of HIRDLS and SABER total (absolute) gravity wave drag have been derived from vertical gradients of the observed momentum fluxes. In altitude-time cross sections the observed gravity wave drag closely follows the QBO zonal wind shear seen in the ERA-Interim reanalysis of the European Centre for Medium-Range Weather Forecasts (ECMWF). We have also derived the missing drag in the tropical momentum budget of ERA-Interim. This missing drag can be attributed to the contribution of gravity waves in the momentum budget. The ERA-Interim missing drag is considerably stronger than the drag due to planetary waves during QBO westward wind shear and still somewhat stronger during eastward wind shear. This is qualitatively in good agreement with previous considerations that gravity waves are more important for the driving of the QBO than planetary waves [e.g., *Dunkerton*, 1997; *Ern and Preusse*, 2009a, 2009b]. The relative importance of gravity waves and planetary waves in driving the QBO is, however, likely altitude dependent.

The observed gravity wave drag was also compared to absolute values of the ERA-Interim missing drag. Very good agreement is found in the relative variations. A minor shift in altitude between observed peak gravity wave drag and ERA-Interim missing drag can be explained by the observational filter of the HIRDLS

and SABER instruments. During QBO eastward wind shear, there is even good agreement between the peak values of observed HIRDLS and SABER gravity wave drag on the one hand and absolute ERA-Interim missing drag on the other hand (about 0.4 m/s/d). This agreement is better than expected because HIRDLS and SABER are only sensitive to gravity waves with horizontal wavelengths longer than 100-200 km, and also gravity waves with shorter horizontal wavelengths should contribute to the driving of the QBO. During westward wind shear, however, peak values of absolute ERA-Interim missing drag can be as strong as 0.6 m/s/d, i.e., almost twice the observed HIRDLS and SABER drag.

In the ERA-Interim momentum budget the zonal wind tendency $\partial\overline{u}/\partial t$, as well as the drag due to planetary waves, is presumably better constrained by assimilated data than the residual circulations that enter the advection terms in ERA-Interim. Therefore, the fact that the observational data fit well to the ERA-Interim missing drag for the QBO eastward wind reversals, but not so well for the westward wind reversals, might hint at uncertainties in the ERA-Interim advection terms. For example, advection terms can be quite strong, even if the zonal wind tendency itself is very weak. In particular during westward wind shear, strong peaks of the advection terms have to be compensated by missing (gravity wave) drag that is much stronger than in the observations. During eastward wind reversals the advection terms partly counteract the wind tendency, maybe resulting in too weak missing drag in ERA-Interim and therefore a too close match with the magnitude of the observed drag.

Also, a comparison with recent QBO model simulations shows that even though there is qualitatively good agreement in the relative variations of the different terms of the tropical momentum budget, there is still no fully consistent picture of the driving of the QBO. In particular, the role of short horizontal wavelength (<100 km) gravity waves is still an open issue. If these waves contribute significantly to the driving of the QBO, gravity waves would be even more important in the QBO momentum budget than already indicated by the part of the gravity wave spectrum visible for instruments like HIRDLS and SABER. Further, there seems to be still some uncertainty in the horizontal and vertical advection terms of the momentum budget. This is not only the case for QBO model simulations but also for reanalysis data sets: in the lower and middle stratosphere, the vertical velocity $\overline{w}^*$ varies strongly between different reanalysis data sets [e.g., *Seviour et al.*, 2012].

Another open issue is the intermittency of gravity waves: the distribution of gravity waves in the real atmosphere is a mixture of strong and weak events and not uniform like the source distributions of many gravity wave parameterizations used in GCMs and CCMs. There are indications that simulations of the QBO could significantly benefit from including this effect [*Lott et al.*, 2012]. Therefore, we have also investigated the intermittency of gravity wave momentum fluxes in the tropics. We found that in the tropics the distribution of gravity waves is not as intermittent as, for example, in the southern polar vortex [e.g., *Hertzog et al.*, 2012]. Still, the intermittency in the tropics is quite strong. For example, during both QBO eastward and westward wind phases the 10% strongest gravity wave events contribute more than 35% to the total observed momentum fluxes at 20 km altitude.

Even though there are some limitations in the observed HIRDLS and SABER gravity wave data sets (large errors and limited spectral coverage), the derived gravity wave variances, total (absolute) momentum fluxes, and drag give a very consistent picture of the gravity wave contribution to the zonal momentum budget in the tropics. In particular, by comparing our observations to ERA-Interim and model simulations, it is indicated that the horizontal and vertical advection terms are likely one of the main uncertainties in the tropical momentum budget. This shows that there is still a considerable lack of understanding about details of the forcing of the QBO. Our results can therefore be some guidance for future model studies that are needed for a more realistic representation of the QBO in GCMs/CCMs.

Appendix A: MEM/HA Results for Single Altitude Profiles

To illustrate the capabilities of the MEM/HA method introduced by *Preusse et al.* [2002], Figure A1 shows several HIRDLS altitude profiles for both QBO eastward wind shear (Figures A1a, A1c, and A1e) and QBO westward wind shear (Figures A1b, A1d, and A1f) at 30 km altitude. In Figures A1a, A1c, and A1e (Figures A1b, A1d, and A1f) the QBO zonal wind is directed westward (eastward) below 30 km altitude. Directly above 30 km, winds are opposite, and at 30 km altitude the zonal wind is about 0. Altitude profiles in Figures A1a, A1c, and A1e are from October 2005 and October 2007, and altitude profiles in Figures A1b,

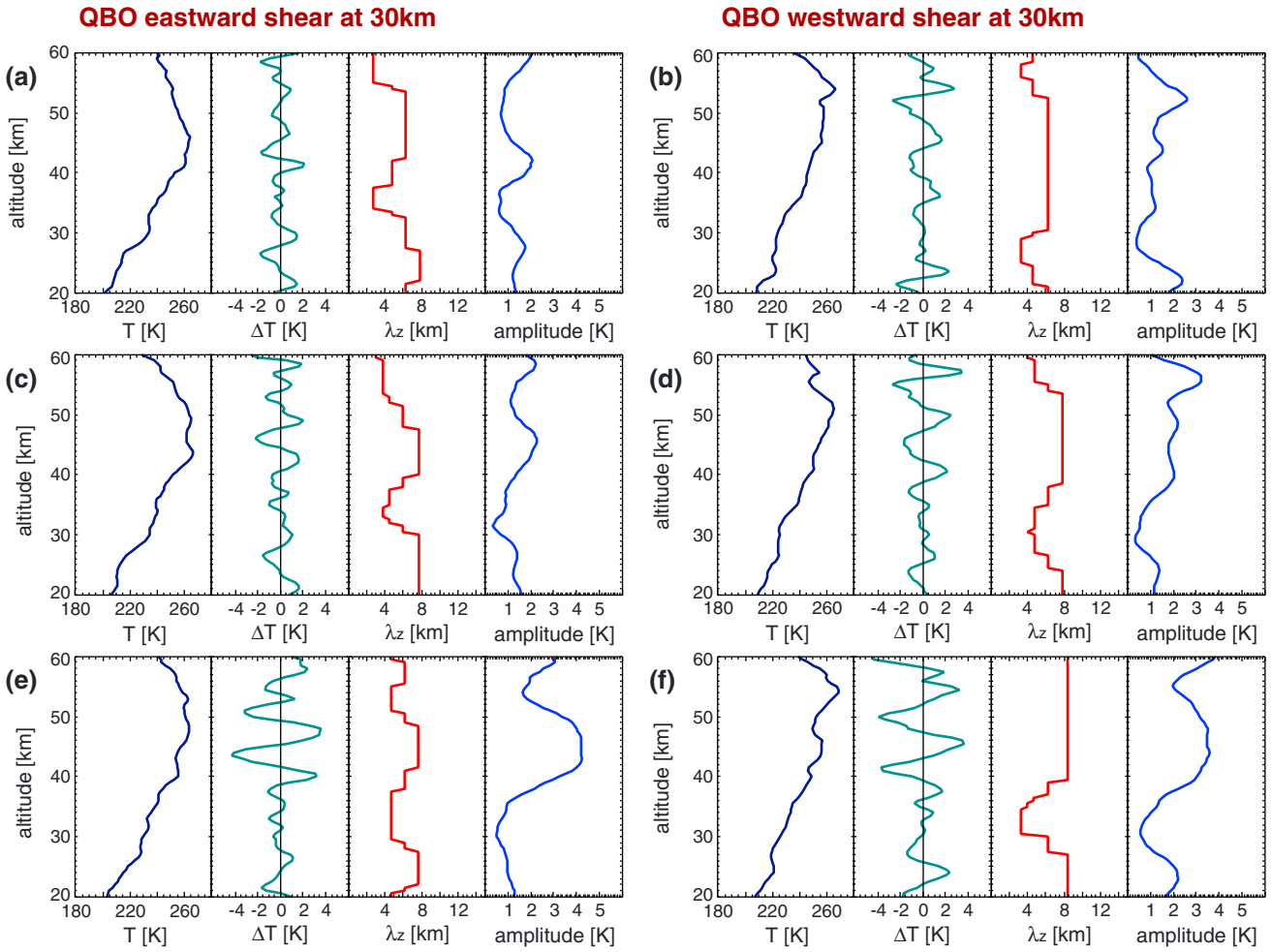

Figure A1. Several examples of HIRDLS temperature altitude profiles and temperature perturbations (ΔT) due to gravity waves with vertical wavelengths λ_z<12 km are displayed, as well as the gravity wave vertical wavelengths and temperature amplitudes resulting from the MEM/HA method for the dominant wave at each altitude. (a, c, and e) QBO eastward zonal wind shear at 30 km altitude. (b, d, and f) QBO westward zonal wind shear at 30 km altitude.

A1d, and A1f are from July and August 2006. All altitude profiles are from the latitude band 5°S–5°N. In each of Figures A1a–A1f the dark blue curves show the original HIRDLS temperature profiles. The teal curve in each of Figures A1a–A1f shows the temperature perturbations due to gravity waves with vertical wavelengths λ_z <12 km, and the red and the bright blue curves show altitude profiles of vertical wavelengths and gravity wave amplitudes obtained from these temperature perturbations using the MEM/HA method with a 5 km vertical window. In all cases displayed in Figure A1 upward propagating gravity waves dissipate in the altitude region around 30 km, likely due to critical level filtering. While approaching their dissipation altitude both their amplitude and their vertical wavelength are more and more reduced. This is well captured in the MEM/HA amplitudes and vertical wavelengths, which both minimize at the dissipation altitude.

It should be mentioned that in the altitude profiles shown in Figure A1 different wave packets are seen in different altitude ranges. While one wave packet obviously dissipates at around 30 km altitude, other wave packets, likely due to different waves, are seen at higher altitudes.

This finding is as expected, and there are several mechanisms that can lead to these observed features. First, as seen in Figure A1, one wave packet can dissipate when it approaches a critical level. Above this critical level (in the changed background winds) other waves will find improved propagation conditions, and accordingly their amplitude can grow substantially. This could be the case in Figure A1 above 30 km altitude.

There are, however, also other processes that will lead to the formation of wave packets. For example, gravity wave sources are very intermittent and usually do not act continuously over longer time periods. Therefore,

gravity waves are excited as wave packets of limited vertical extent that propagate upward with the vertical group velocity c_{gz}. For medium-frequency gravity waves we obtain

$$|c_{gz}| = \frac{N}{2\pi}\frac{\lambda_z^2}{\lambda_h} \tag{A1}$$

[cf. *Fritts and Alexander*, 2003, equations (32) and (34)]. Assuming, for example, typical values of $\lambda_z = 8$ km and $\lambda_h = 800$ km for vertical and horizontal wavelength, typical group velocities for gravity waves observable from limb-viewing satellite instruments are of the order of about 1 km/h. As a consequence, it cannot be expected that the same wave is seen in the whole altitude range of an altitude profile. Another process that could lead to wave packet-like structures in observed altitude profiles could be nonvertical propagation of gravity waves. These effects are also frequently seen in radiosonde observations and have been discussed in detail, for example, by *Sato et al.* [2003]. This also shows that to investigate the driving of the QBO by gravity waves, it is required to average over a large number of single observations, which is possible for the satellite data sets presented in our study.

Overall, the vertical structure of temperature perturbations in an observed altitude profile can be very complicated. The results presented in Figure A1, however, show that the MEM/HA method provides reliable values of gravity wave amplitudes and vertical wavelengths over the whole altitude range.

Appendix B: Gravity Wave Momentum Flux Spectra

In section 3.1 the assumption was made that only gravity waves with vertical wavelengths <12 km should contribute to the QBO. In order to check whether this assumption holds, we now calculate gravity wave momentum flux spectra directly below and directly above QBO wind reversals to find out which part of the spectrum is affected the most by the wind reversal. Like in *Ern and Preusse* [2012], we use HIRDLS data for the estimation of the spectra, because HIRDLS data offer a better statistics than SABER to sample the spectral domain of horizontal and vertical wave numbers. Further, the HIRDLS horizontal sampling step is about 90 km, corresponding to a shortest resolved along-track wavelength of 180 km. Given the visibility limits of a limb sounder, aliasing effects therefore should be small. In addition, HIRDLS is sensitive to shorter vertical wavelengths than SABER (as short as about 2 km).

To cover a vertical wavelength range as large as possible, the estimation of gravity wave spectra is carried out for a momentum flux analysis based on 10 km vertical windows. This analysis covers vertical wavelengths λ_z <25 km (see also *Ern et al.* [2011]). The use of such large vertical windows, however, strongly constrains the altitudes and time periods when the estimation of spectra makes sense: we have to find time periods when the two QBO wind bands, one above and the other below the zero zonal wind line, are larger in their vertical extent than the 10 km needed for our analysis. Further, we are limited to the altitude range 20–40 km where the QBO is situated. Therefore, the zero zonal wind line should be located at around 30 km altitude.

Still, it is possible to approximately match all these criteria for QBO wind reversals in both directions. For the case of QBO eastward wind shear at 30 km we calculate gravity wave momentum flux spectra averaged over the months October 2005 and October 2007, and for QBO westward wind shear spectra are calculated for the period July/August 2006.

The results are shown in Figure B1. Figures B1a, B1b, and B1c (Figures B1d, B1e, and B1f) are for the westward to eastward (eastward to westward) QBO wind reversal. Figures B1a and B1d show the momentum flux spectra representing the altitude interval 20–30 km (i.e., below the wind reversal), and Figures B1b and B1e show the spectra for the altitude interval 30–40 km (i.e., above the wind reversal). Figures B1c and B1f show the difference of the spectra below and above the wind reversal. The spectral bins used in our analysis are the same as in *Ern and Preusse* [2012]: we use overlapping square bins with a full width of 0.2 in units of the logarithmic axes in Figure B1 (for both *x* and *y* directions). The step width of the rectangular grid used is 0.1 in both directions.

By comparing the spectra below and above the wind reversal, we find for both cases (QBO eastward and westward wind shear) that in the spectra in Figures B1b and B1e (above the wind reversal) the momentum flux is strongly reduced at vertical wavelengths λ_z <10 km (i.e., particularly at intrinsic phase speeds

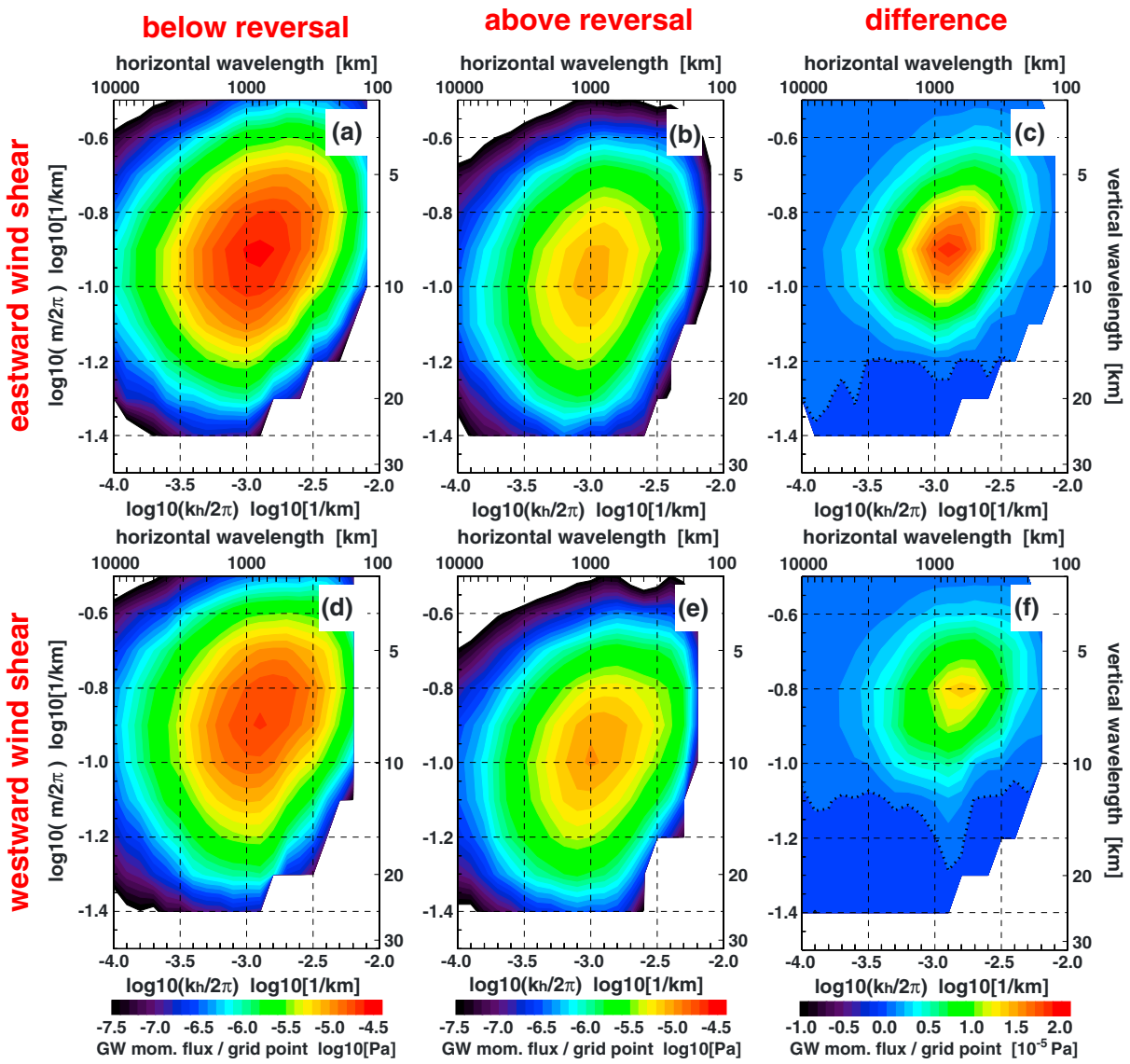

Figure B1. HIRDLS gravity wave momentum flux spectra for periods when the QBO zero wind line is at about 30 km altitude: (a) spectrum for 20–30 km altitude (i.e., below the QBO westward to eastward wind reversal), (b) spectrum for 30–40 km altitude (i.e., above the wind reversal), (c) the difference Figure B1a minus Figure B1b. Please note that in Figures B1a and B1b a logarithmic momentum flux color scale is used, but in Figure B1c a linear momentum flux color scale is used. (d–f) Same as Figures B1a–B1c but for QBO eastward to westward wind reversal. The dotted lines in Figures B1c and B1f are the lines of zero momentum flux difference.

$\hat{c}$ <30 m/s). This is also found in the differences between lower and upper level spectra (Figures B1c and B1f), and indicated by values in the green and red color range of the linear momentum flux color scale. Please note that the step width of the 2-D grid used for Figure B1 is 0.1, and the momentum flux differences are already quite low in Figures B1c and B1f at $\log_{10}(m/2\pi) = -1.1$ (in units of $\log_{10}$(1/km)), corresponding to a vertical wavelength of λ_z =12.6 km. The color shading between −1.0 and −1.1 is just an interpolation of the graphics software. This means that there is only little change in the momentum fluxes at vertical wavelengths >10 km: for HIRDLS (SABER), less than 10% (20%) of the momentum flux difference between lower and upper level is at vertical wavelengths >10 km. These findings support our theoretical considerations in section 3.1: the main driving of the QBO by gravity waves can be estimated from the dissipation of gravity waves with vertical wavelengths shorter than about 12 km. The filtering of these shorter-scale waves is also consistent with the assumption that critical level filtering is the main driver of the QBO.

The small error arising from the 12 km vertical wavelength cutoff can be neglected if compared to other known error sources. In particular, it has been found by *Gong et al.* [2012] that in the tropics QBO-related

variations of gravity wave variances seen by the Atmospheric Infrared Sounder (AIRS) instrument are much weaker than seasonal variations. Therefore, it has been concluded by *Gong et al.* [2012] that the gravity waves visible for the AIRS instrument (only vertical wavelengths >12 km) contribute only little to the forcing of the QBO, which is another indication that the limitation of our study to vertical wavelengths <12 km will not introduce large errors. Of course, due to their observational filter, HIRDLS and SABER are not sensitive to gravity waves with horizontal wavelengths shorter than about 100–200 km [see also *Ern et al.*, 2005]. Therefore, the part of the QBO driving that is due to these short horizontal wavelength gravity waves is not covered by our study. Possibly, gravity waves with short horizontal wavelengths (<100 km) do not contribute much to the driving of the QBO because they might dissipate at higher altitudes. Nevertheless, our values of momentum fluxes and gravity wave drag will likely be lower limits of the gravity wave contribution to the QBO driving.

Acknowledgments
ERA-Interim data were obtained from ECMWF. SABER data were provided by GATS Inc., and HIRDLS data by NASA. Many thanks also go to the teams of the HIRDLS and SABER instruments for their continued effort. Very helpful comments by Marvin Geller and two anonymous reviewers are gratefully acknowledged.

References

Alexander, M. J., and K. H. Rosenlof (2003), Gravity-wave forcing in the stratosphere: Observational constraints from the Upper Atmosphere Research Satellite and implications for parameterization in global models, *J. Geophys. Res.*, *108*, 4597, doi:10.1029/2003JD003373.

Alexander, M. J., et al. (2008), Global estimates of gravity wave momentum flux from High Resolution Dynamics Limb Sounder observations, *J. Geophys. Res.*, *113*, D15S18, doi:10.1029/2007JD008807.

Alexander, M. J., et al. (2010), Recent developments in gravity-wave effects in climate models and the global distribution of gravity-wave momentum flux from observations and models, *Q. J. R. Meteorolog. Soc.*, *136*, 1103–1124, doi:10.1002/qj.637.

Andrews, D. G., J. R. Holton, and C. B. Leovy (1987), *Middle Atmosphere Dynamics*, 489 pp., Academic Press, Orlando, FL.

Baldwin, M. P., et al. (2001), The quasi-biennial oscillation, *Rev. Geophys.*, *39*, 179–229.

Barnett, J. J., C. L. Hepplewhite, S. Osprey, J. C. Gille, and R. Khosravi (2008), Cross-validation of HIRDLS and COSMIC radio-occultation retrievals, particularly in relation to fine vertical structure, *Proc. SPIE Int. Soc. Opt. Eng.*, *7082*, 708216, doi:10.1117/12.800702.

Boer, G. J., and K. Hamilton (2008), QBO influence on extratropical predictive skill, *Clim. Dyn.*, *31*, 987–1000, doi:10.1007/s00382-008-0379-5.

Choi, H.-J., H.-Y. Chun, J. Gong, and D. L. Wu (2012), Comparison of gravity wave temperature variances from ray-based spectral parameterization of convective gravity wave drag with AIRS observations, *J. Geophys. Res.*, *117*, D05115, doi:10.1029/2011JD016900.

Dee, D. P., et al. (2011), The ERA-Interim reanalysis: Configuration and performance of the data assimilation system, *Q. J. R. Meteorolog. Soc.*, *137*, 553–597, doi:10.1002/qj.828.

de la Torre, A., T. Schmidt, and J. Wickert (2006), A global analysis of wave potential energy in the lower and middle atmosphere from CHAMP and SAC-C GPS-RO long term data, *Geophys. Res. Lett.*, *33*, L24809, doi:10.1029/2006GL027696.

Dunkerton, T. J. (1997), The role of gravity waves in the quasi-biennial oscillation, *J. Geophys. Res.*, *102*, 26,053–26,076.

Ebdon, R. A. (1975), The quasi-biennial oscillation and its association with tropospheric circulation patterns, *Meteorol. Mag.*, *104*, 282–297.

Ern, M., and P. Preusse (2009a), Wave fluxes of equatorial Kelvin waves and QBO zonal wind forcing derived from SABER and ECMWF temperature space-time spectra, *Atmos. Chem. Phys.*, *9*, 3957–3986, doi:10.5194/acp-9-3957-2009.

Ern, M., and P. Preusse (2009b), Quantification of the contribution of equatorial Kelvin waves to the QBO wind reversal in the stratosphere, *Geophys. Res. Lett.*, *36*, L21801, doi:10.1029/2009GL040493.

Ern, M., and P. Preusse (2012), Gravity wave momentum flux spectra observed from satellite in the summertime subtropics: Implications for global modeling, *Geophys. Res. Lett.*, *39*, L15810, doi:10.1029/2012GL052659.

Ern, M., P. Preusse, M. J. Alexander, and C. D. Warner (2004), Absolute values of gravity wave momentum flux derived from satellite data, *J. Geophys. Res.*, *109*, D20103, doi:10.1029/2004JD004752.

Ern, M., P. Preusse, and C. D. Warner (2005), A comparison between CRISTA satellite data and Warner and McIntyre gravity wave parameterization scheme: Horizontal and vertical wavelength filtering of gravity wave momentum flux, *Adv.Space Res.*, *35*, 2017–2023, doi:10.1016/j.asr.2005.04.109.

Ern, M., P. Preusse, M. Krebsbach, M. G. Mlynczak, and J. M. Russell III (2008), Equatorial wave analysis from SABER and ECMWF temperatures, *Atmos. Chem. Phys.*, *8*, 845–869, doi:10.5194/acp-8-845-2008.

Ern, M., C. Lehmann, M. Kaufmann, and M. Riese (2009a), Spectral wave analysis at the mesopause from SCIAMACHY airglow data compared to SABER temperature spectra, *Ann. Geophys.*, *27*, 407–416.

Ern, M., H.-K. Cho, P. Preusse, and S. D. Eckermann (2009b), Properties of the average distribution of equatorial Kelvin waves investigated with the GROGRAT ray tracer, *Atmos. Chem. Phys.*, *9*, 7973–7995, doi:10.5194/acp-9-7973-2009.

Ern, M., P. Preusse, J. C. Gille, C. L. Hepplewhite, M. G. Mlynczak, J. M. Russell III, and M. Riese (2011), Implications for atmospheric dynamics derived from global observations of gravity wave momentum flux in stratosphere and mesosphere, *J. Geophys. Res.*, *116*, D19107, doi:10.1029/2011JD015821.

Ern, M., C. Arras, A. Faber, K. Fröhlich, Ch. Jacobi, S. Kalisch, M. Krebsbach, P. Preusse, T. Schmidt, and J. Wickert (2013a), Observations and ray tracing of gravity waves: Implications for global modeling, in *Climate and Weather of the Sun-Earth System (CAWSES): Highlights from a Priority Program*, edited by F.-J. Lübken, pp. 383–408, Springer, Dordrecht, The Netherlands, doi:10.1007/978-94-007-4348-9_21.

Ern, M., P. Preusse, S. Kalisch, M. Kaufmann, and M. Riese (2013b), Role of gravity waves in the forcing of quasi two-day waves in the mesosphere: An observational study, *J. Geophys. Res. Atmos.*, *118*, 3467–3485, doi:10.1029/2012JD018208.

Evan, S., M. J. Alexander, and J. Dudhia (2012), WRF simulations of convectively generated gravity waves in opposite QBO phases, *J. Geophys. Res.*, *117*, D12117, doi:10.1029/2011JD017302.

Forbes, J. M., X. Zhang, S. E. Palo, J. M. Russell III, C. J. Mertens, and M. G. Mlynczak (2009), Kelvin waves in the stratosphere, mesosphere and lower thermosphere temperatures as observed by TIMED SABER during 2002–2006, *Earth Planets Space*, *61*, 447–453.

Fritts, D. C., and M. J. Alexander (2003), Gravity wave dynamics and effects in the middle atmosphere, *Rev. Geophys.*, *41*(1), 1003, doi:10.1029/2001RG000106.

Geller, M. A., et al. (2013), A comparison between gravity wave momentum fluxes in observations and climate models, *J. Clim.*, *26*, 6383–6405, doi:10.1175/JCLI-D-12-00545.1.

Gerber, E. P., et al. (2012), Assessing and understanding the impact of stratospheric dynamics and variability on the Earth system, *Bull. Am. Meteorol. Soc.*, *93*, 845–859, doi:10.1175/BAMS-D-11-00145.1.

Gille, J. C., J. J. Barnett, J. Whitney, M. Dials, D. Woodard, W. Rudolf, A. Lambert, and W. Mankin (2003), The high resolution dynamics limb sounder (HIRDLS) experiment on Aura, *Proc. SPIE Int. Soc. Opt. Eng.*, *5152*, 162–171.

Gille, J. C., et al. (2008), High resolution dynamics limb sounder: Experiment overview, recovery, and validation of initial temperature data, *J. Geophys. Res.*, *113*, D16S43, doi:10.1029/2007JD008824.

Gille, J. C., et al. (2011), High Resolution Dynamics Limb Sounder Earth Observing System (EOS): Data description and quality, Version 6 (V6). [Document available at: http://disc.sci.gsfc.nasa.gov/data-holdings.]

Giorgetta, M. A., E. Manzini, and E. Roeckner (2002), Forcing of the quasi-biennial oscillation from a broad spectrum of atmospheric waves, *Geophys. Res. Lett.*, *29*, 1245, doi:10.1029/2002GL014756.

Giorgetta, M. A., E. Manzini, E. Roeckner, M. Esch, and L. Bengtsson (2006), Climatology and forcing of the Quasi-Biennial Oscillation in the MAECHAM5 model, *J. Clim.*, *19*, 3882–3901.

Gong, J., M. A. Geller, and L. Wang (2008), Source spectra information derived from U.S. high-resolution radiosonde data, *J. Geophys. Res.*, *113*, D10106, doi:10.1029/2007JD009252.

Gong, J., D. L. Wu, and S. D. Eckermann (2012), Gravity wave variances and propagation derived from AIRS radiances, *Atmos. Chem. Phys.*, *12*, 1701–1720, doi:10.5194/acp-12-1701-2012.

Gray, L. J., et al. (2010), Solar influences on climate, *Rev. Geophys.*, *48*, RG4001, doi:10.1029/2009RG000282.

Hertzog, A., G. Boccara, R. A. Vincent, F. Vial, and P. Cocquerez (2008), Estimation of gravity-wave momentum flux and phase speeds from quasi-Lagrangian stratospheric balloon flights: 2. Results from the Vorcore campaign in Antarctica, *J. Atmos. Sci.*, *65*, 3056–3070.

Hertzog, A., M. J. Alexander, and R. Plougonven (2012), On the intermittency of gravity wave momentum flux in the stratosphere, *J. Atmos. Sci.*, *69*, 3433–3448.

Holton, J. R., and R. S. Lindzen (1972), An updated theory for the quasi-biennial cycle of the tropical stratosphere, *J. Atmos. Sci.*, *29*, 1076–1080.

Holton, J. R., and H.-C. Tan (1980), The influence of the equatorial quasi-biennial oscillation on the global circulation at 50 mb, *J. Atmos. Sci.*, *37*, 2200–2208.

Kawatani, Y., K. Sato, T. J. Dunkerton, S. Watanabe, S. Miyahara, and M. Takahashi (2010), The roles of equatorial trapped waves and internal inertia gravity waves in driving the quasi-biennial oscillation. Part I: Zonal mean wave forcing, *J. Atmos. Sci.*, *67*, 963–980, doi:10.1175/2009JAS3222.1.

Kim, Y.-H., A. C. Bushell, D. R. Jackson, and H.-Y. Chun (2013), Impacts of introducing a convective gravity-wave parameterization upon the QBO in the Met Office Unified Model, *Geophys. Res. Lett.*, *40*, 1873–1877, doi:10.1002/grl.50353.

Krebsbach, M., and P. Preusse (2007), Spectral analysis of gravity wave activity in SABER temperature data, *Geophys. Res. Lett.*, *34*, L03814, doi:10.1029/2006GL028040.

Lehmann, C. I., Y.-H. Kim, P. Preusse, H.-Y. Chun, M. Ern, and S.-Y. Kim (2012), Consistency between Fourier transform and small-volume few-wave decomposition for spectral and spatial variability of gravity waves above a typhoon, *Atmos. Meas. Tech.*, *5*, 1637–1651, doi:10.5194/amt-5-1637-2012.

Lindzen, R. S. (1981), Turbulence and stress owing to gravity wave and tidal breakdown, *J. Geophys. Res.*, *86*, 9707–9714.

Lindzen, R. S., and J. R. Holton (1968), A theory of the quasi-biennial oscillation, *J. Atmos. Sci.*, *25*, 1095–1107.

Lott, F., L. Guez, and P. Maury (2012), A stochastic parameterization of non-orographic gravity waves: Formalism and impact on the equatorial stratosphere, *Geophys. Res. Lett.*, *39*, L06807, doi:10.1029/2012GL051001.

Marshall, A. G., and A. A. Scaife (2009), Impact of the QBO on surface winter climate, *J. Geophys. Res.*, *114*, D18110, doi:10.1029/2009JD011737.

Mlynczak, M. G. (1997), Energetics of the mesosphere and lower thermosphere and the SABER instrument, *Adv. Space Res.*, *44*, 1177–1183.

Monier, E., and B. C. Weare (2011), Climatology and trends in the forcing of the stratospheric zonal-mean flow, *Atmos. Chem. Phys.*, *11*, 12,751–12,771, doi:10.5194/acp-11-12751-2011.

Orr, A., P. Bechtold, J. F. Scinocca, M. Ern, and M. Janiskova (2010), Improved middle atmosphere climate and forecasts in the ECMWF model through a nonorographic gravity wave drag parameterization, *J. Clim.*, *23*, 5905–5926, doi:10.1175/2010JCLI3490.1.

Preusse, P., A. Dörnbrack, S. D. Eckermann, M. Riese, B. Schaeler, J. T. Bacmeister, D. Broutman, and K. U. Grossmann (2002), Space-based measurements of stratospheric mountain waves by CRISTA, 1. Sensitivity, analysis method, and a case study, *J. Geophys. Res.*, *107*(D23), 8178, doi:10.1029/2001JD000699.

Preusse, P., S. Schroeder, L. Hoffmann, M. Ern, F. Friedl-Vallon, H. Oelhaf, H. Fischer, and M. Riese (2009), New perspectives on gravity wave remote sensing by spaceborne infrared limb imaging, *Atmos. Meas. Tech.*, *2*, 299–311.

Randel, W. J., and F. Wu (2005), Kelvin wave variability near the equatorial tropopause observed in GPS radio occultation measurements, *J. Geophys. Res.*, *110*, D03102, doi:10.1029/2004JD005006.

Ratnam, M. V., T. Tsuda, T. Kozu, and S. Mori (2006), Long-term behavior of the Kelvin waves revealed by CHAMP/GPS RO measurements and their effect on the tropopause structure, *Ann. Geophys.*, *24*, 1355–1366.

Remsberg, E. E., L. L. Gordley, B. T. Marshall, R. E. Thompson, J. Burton, P. Bhatt, V. L. Harvey, G. Lingenfelser, and M. Natarajan (2004), The Nimbus 7 LIMS version 6 radiance conditioning and temperature retrieval methods and results, *J. Quant. Spectrosc. Radiat. Transfer*, *86*, 395–424, doi:10.1016/j.jqsrt.2003.12.007.

Remsberg, E. E., et al. (2008), Assessment of the quality of the Version 1.07 temperature-versus-pressure profiles of the middle atmosphere from TIMED/SABER, *J. Geophys. Res.*, *113*, D17101, doi:10.1029/2008JD010013.

Richter, J. H., F. Sassi, and R. R. Garcia (2010), Toward a physically based gravity wave source parameterization in a general circulation model, *J. Atmos. Sci.*, *67*, 136–156.

Russell, J. M., III, M. G. Mlynczak, L. L. Gordley, J. Tansock, and R. Esplin (1999), An overview of the SABER experiment and preliminary calibration results, *Proc. SPIE Int. Soc. Opt. Eng.*, *3756*, 277–288.

Sato, K., M. Yamamori, S.-Y. Ogino, N. Takahashi, Y. Tomikawa, and T. Yamanouchi (2003), A meridional scan of the stratospheric gravity wave field over the ocean in 2001 (MeSSO2001), *J. Geophys. Res.*, *108*(D16), 4491, doi:10.1029/2002JD003219.

Scaife, A., N. Butchart, C. D. Warner, D. Stainforth, and W. Norton (2000), Realistic quasi-biennial oscillations in a simulation of the global climate, *Geophys. Res. Lett.*, *27*, 3481–3484.

Schroeder, S., P. Preusse, M. Ern, and M. Riese (2009), Gravity waves resolved in ECMWF and measured by SABER, *Geophys. Res. Lett.*, *36*, L10805, doi:10.1029/2008GL037054.

Seviour, W. J. M., N. Butchart, and S. C. Hardiman (2012), The Brewer-Dobson circulation inferred from ERA-Interim, *Q. J. R. Meteorolog. Soc.*, *138*, 878–888, doi:10.1002/qj.966.

Song, I.-S., H.-Y. Chun, R. R. Garcia, and B. A. Boville (2007), Momentum flux spectrum of convectively forced inertial gravity waves and its application to gravity wave drag parameterization. Part II: Impact in a GCM (WACCM), *J. Atmos. Sci.*, *64*, 2286–2308.

Ungermann, J., L. Hoffmann, P. Preusse, M. Kaufmann, and M. Riese (2010), Tomographic retrieval approach for mesoscale gravity wave observations by the PREMIER Infrared Limb-Sounder, *Atmos. Meas. Tech.*, *3*, 339–354.

Warner, C. D., A. A. Scaife, and N. Butchart (2005), Filtering of parameterized nonorographic gravity waves in the Met Office unified model, *J. Atmos. Sci.*, *62*, 1831–1848.

Wright, C. J., S. M. Osprey, J. J. Barnett, L. J. Gray, and J. C. Gille (2010), High resolution dynamics limb sounder measurements of gravity wave activity in the 2006 Arctic stratosphere, *J. Geophys. Res.*, *115*, D02105, doi:10.1029/2009JD011858.

Wright, C. J., M. B. Rivas, and J. C. Gille (2011), Intercomparisons of HIRDLS, COSMIC and SABER for the detection of stratospheric gravity waves, *Atmos. Meas. Tech.*, *4*, 1581–1591, doi:10.5194/amt-4-1581-2011.

Wright, C. J., S. M. Osprey, and J. C. Gille (2013), Global observations of gravity wave intermittency and its impact on the observed momentum flux morphology, *J. Geophys. Res. Atmos.*, *118*, 10,980–10,993, doi:10.1002/jgrd.50869.

Wu, D. L., and S. D. Eckermann (2008), Global gravity wave variances from Aura MLS: Characteristics and interpretation, *J. Atmos. Sci.*, *65*, 3695–3718.

Xue, X.-H., H.-L. Liu, and X.-K. Dou (2012), Parameterization of the inertial gravity waves and generation of the quasi-biennial oscillation, *J. Geophys. Res.*, *117*, D06103, doi:10.1029/2011JD016778.

Yang, G.-Y., B. Hoskins, and L. J. Gray (2012), The influence of the QBO on the propagation of equatorial waves into the stratosphere, *J. Atmos. Sci.*, *69*, 2959–2982.